

Crustal Seismogenic Thickness and Thermal Structure of NW South America

Angela Maria Gomez Garcia¹, Álvaro González², Mauro Cacace³, Magdalena Scheck-Wenderoth¹, and Gaspar Monsalve⁴

¹Helmholtz Centre Potsdam, GFZ German Research Centre For Geosciences

²Centre de Recerca Matemàtica

³Helmholtz Centre Potsdam

⁴Universidad Nacional de Colombia

November 30, 2022

Abstract

The crustal seismogenic thickness (CST) has direct implications on the magnitude and occurrence of crustal earthquakes, and therefore, on the seismic hazard of high-populated regions. Amongst other factors, the seismogenesis of rocks is affected by in-situ conditions (temperature and state of stress) and by their heterogeneous composition. Diverse laboratory experiments have explored the frictional behavior of the most common materials forming the crust and upper most mantle, which are limited to the scale of the investigated sample. However, a workflow to up-scale and validate these experiments to natural geological conditions of crustal and upper mantle rocks is lacking. We used NW South America as a case-study to explore the spatial variation of the CST and the potential temperatures at which crustal earthquakes occur, computing the 3D steady-state thermal field taking into account lithology-constrained thermal parameters. Modelled hypocentral temperatures show a general agreement with the seismogenic windows of rocks and mineral assemblies expected in the continental crust. A few outliers in the hypocentral temperatures showcase nucleation conditions consistent with the seismogenic window of olivine-rich rocks, and are interpreted in terms of uncertainties in the Moho depths and/or in the earthquake hypocenters, or due to the presence of ultramafic rocks within the allochthonous crustal terranes accreted to this complex margin. Our results suggest that the two largest earthquakes recorded in the region (Murindo sequence, in 1992) nucleated at the lower boundary of the seismogenic crust, highlighting the importance of considering this transition into account when characterizing seismogenic sources for hazard assessments.

Hosted file

gomez-garcia_etal_jgr_caribbeanearthquakes_supinfo.docx available at <https://authorea.com/users/559757/articles/608151-crustal-seismogenic-thickness-and-thermal-structure-of-nw-south-america>

Crustal Seismogenic Thickness and Thermal Structure of NW South America

Ángela María Gómez-García^{1,2}, Álvaro González^{1,3}, Mauro Cacace¹, Magdalena Scheck-Wenderoth¹, Gaspar Monsalve⁴

¹ GFZ German Research Centre for Geosciences. Telegrafenberg, 14473, Potsdam, Germany.

² Corporation Center of Excellence in Marine Sciences (CEMarin). Bogotá, Colombia.

³ Centre de Recerca Matemàtica (CRM). Campus UAB, Edifici C. 08193, Bellaterra (Barcelona), Spain.

⁴ Universidad Nacional de Colombia, Facultad de Minas, Medellín, Colombia.

Corresponding author: Ángela María Gómez-García (angela@gfz-potsdam.de)

Key Points:

- We propose a workflow for contrasting temperatures for crustal seismogenesis provided by laboratory experiments.
- The majority of the crustal seismic events have modelled hypocentral temperatures of less than 350°C.
- A thick lower crust, allochthonous terranes and a hot upper mantle could explain hypocentral temperatures >600°C.

18 Abstract

19 The crustal seismogenic thickness (CST) has direct implications on the magnitude and occurrence
20 of crustal earthquakes, and therefore, on the seismic hazard of high-populated regions. Amongst
21 other factors, the seismogenesis of rocks is affected by in-situ conditions (temperature and state of
22 stress) and by their heterogeneous composition. Diverse laboratory experiments have explored the
23 frictional behavior of the most common materials forming the crust and upper most mantle, which
24 are limited to the scale of the investigated sample. However, a workflow to up-scale and validate
25 these experiments to natural geological conditions of crustal and upper mantle rocks is lacking.
26 We used NW South America as a case-study to explore the spatial variation of the CST and the
27 potential temperatures at which crustal earthquakes occur, computing the 3D steady-state thermal
28 field taking into account lithology-constrained thermal parameters. Modelled hypocentral
29 temperatures show a general agreement with the seismogenic windows of rocks and mineral
30 assemblies expected in the continental crust. A few outliers in the hypocentral temperatures
31 showcase nucleation conditions consistent with the seismogenic window of olivine-rich rocks, and
32 are interpreted in terms of uncertainties in the Moho depths and/or in the earthquake hypocenters,
33 or due to the presence of ultramafic rocks within the allochthonous crustal terranes accreted to this
34 complex margin. Our results suggest that the two largest earthquakes recorded in the region
35 (Murindó sequence, in 1992) nucleated at the lower boundary of the seismogenic crust,
36 highlighting the importance of considering this transition into account when characterizing
37 seismogenic sources for hazard assessments.

38 Plain Language Summary

39 Earthquake magnitudes are thought to correlate to the area that ruptures at the subsurface during
40 the earthquake occurrence. Understanding the conditions of the rocks at the depths at which
41 seismicity occurs can shed lights in seismic hazard assessments. In particular, using a long record
42 of earthquakes, it is possible to estimate the portions of the solid Earth prone to host earthquakes.
43 Laboratory experiments have significantly advanced our understanding of the rock's behavior
44 during deformation, simulating the conditions found in nature. However, limitations in the
45 experimental conditions that can be tested in a laboratory pose uncertainties when upscaling those
46 results to natural conditions. In this work, we studied northwestern South America to explore the
47 spatial variation of the region hosting earthquakes in terms of their potential temperatures at which
48 crustal earthquakes occur, using a three-dimensional model of the uppermost 75 km of the Earth.
49 Such analyses allow us to better delineate which parts of the Earth's interior can generate
50 earthquakes, and estimating how large these can be, providing important constrains for future
51 assessments of seismic hazard and risk.

52 1 Introduction

53 The crustal seismogenic thickness (CST) encloses the portion of the crust where the
54 majority of earthquakes occur. Its upper boundary, hereafter referred to as the upper stability
55 transition (UST), demarks the onset depth of seismicity. Its lower boundary, referred to as the
56 lower stability transition (LST), defines the cutoff depth of seismicity (Marone & Saffer, 2015;
57 Marone & Scholz, 1988; Scholz, 2019; Wu et al., 2017). The LST can also be used as a

conservative upper estimate of the brittle-ductile transition (BTD) (e.g.: Zuza & Cao, 2020). The depths of both the UST and the LST are usually determined from thresholds (percentiles) of the statistical distribution of earthquake hypocentral depths (e.g.: Marone & Scholz, 1988; Sibson, 1982; Wu et al., 2017). The seismogenic crust is then defined as the portion of the crust that contains a prescribed (i.e., statistically significant) percentage of the recorded earthquakes.

The spatial extend of earthquakes is controlled by the mechanical properties of rocks (which depend on factors such as composition, grain size and mineral assemblies), as well as by the in-situ temperature, pressure and strain rates (Chen et al., 2013; Zielke et al., 2020). Laboratory experiments suggest a range of limiting temperatures for seismogenesis, i.e.: temperatures at which rocks and mineral assemblies exhibit stick-slip behavior as a result of phase transitions. For example, granitic rocks exhibit seismic behavior at temperatures between 90-350°C, gabbro between 200 and 600°C, and olivine gouge between 600 and 1000°C (Scholz, 2019, and references therein). It is generally considered that earthquakes nucleate within the crust at $< 350 \pm 50^\circ\text{C}$, and at $< 700 \pm 100^\circ\text{C}$ in the mantle (see review by Chen et al., 2013).

As an attempt to up-scale the results of laboratory experiments, previous studies have aimed at modelling the thermal field of active systems targeting the temperature ranges at which earthquakes can nucleate (e.g.: Gutscher et al., 2016; Oleskevich et al., 1999; Zuza & Cao, 2020). The results from these efforts suggest that in faults located within the continents, the BDT seems to be controlled by geothermal gradients, being limited by the 300-350°C isotherms, consistent with a quartz-dominated lithology (e.g.: Zuza & Cao, 2020). Nevertheless, most of these approaches usually consider a simplified lithospheric structure, disregarding particular tectonic assemblies that can considerably affect the three-dimensional thermal field of the system. Moreover, most of the discussions about limiting temperatures for seismogenesis have been a-priori undertaken in regions away of subduction zones due to the complexities of such systems (Chen et al., 2013).

In this paper, we explore the CST and the temperatures at which crustal earthquakes nucleate in the South Caribbean and NW South America (Figure 1). Here, the complex tectonic setting poses a challenge to confront the results from laboratory experiments, including the convergence of at least four tectonic plates, the accretion of several allochthonous terranes, and the presence of continental sedimentary basins with thicknesses of up to 8 km (Mora-Bohórquez et al., 2020). Although few events with magnitude $M > 7.0$ have been recorded in northern South America since the deployment of modern seismological networks, there are historical records of earlier great earthquakes, for example, the shock which destroyed the city of Santa Marta, Colombia, in 1834. Similarly, paleoseismological studies in western Venezuela found fault rupture of other events with estimated magnitudes $M > 7.0$ (e.g.: Audemard, 1996; Pousse-Beltran et al., 2018). Overall, there is a substantial seismic hazard in this region (Arcila et al., 2020; Pagani et al., 2018), and large population centers exist close to shallow active faults able to generate devastating earthquakes (Veloza et al., 2012). As a result, there is a high calculated seismic risk (Silva et al., 2018). Therefore, it is expected that a better understanding of the regional seismogenesis will contribute to future seismic hazard and risk assessments.

Here we use the crustal seismic events with the highest quality hypocentral depths reported in the ISC Bulletin since 1980 (International Seismological Centre, 2022) for calculating the depths to the UST, and LST, the CST, and map their spatial variations. We do not attempt to account for a detailed representation of transient changes on the seismogenic zone, but rather focus on a quantification of the regional-scale stability transitions, considering lithological and structural heterogeneities.

As the extend of the CST is influenced by spatially heterogeneous factors such as lithology and local geothermal gradients (Hirth & Beeler, 2015; Zielke et al., 2020), we computed the 3D steady-state thermal response of a recently published gravity-constrained, structural and density model (Gómez-García et al., 2020, 2021). We preferentially target crustal earthquakes given the complexity of the active subduction systems in the study area; therefore, the thermal model considers only the uppermost 75 km. Besides the lithospheric-scale structural model, the main input for our thermal calculations are lithology-dependent thermal properties for the different layers of the lithosphere, the temperature field on the Earth's surface as the upper boundary condition and the temperatures at 75 km depth used as the lower boundary condition. We extracted the temperatures at UST and LST from the 3D thermal model, as well as at the hypocentral depths of the seismic events. This approach has the main advantage of providing a realistic view of the system's heterogeneities, their contribution to the thermal field, and the long-term geological timescale given by the mantle contribution and the realistic lithospheric configuration.

2 Study area

The study area (5° - 15° N and 63° - 82° W, Figure 1) includes the interaction of the Caribbean and Nazca (Coiba) flat-slabs at depth (Gómez-García et al., 2021; Kellogg et al., 2019; Sun et al., 2022). Due to this interaction, a complex tectonic setting is present at lithospheric-scale, including large uncertainties in depths to the Moho interface (e.g.: Avellaneda-Jiménez et al., 2022; Poveda et al., 2015; Reguzzoni & Sampietro, 2015).

Figure 1 depicts the best-located crustal seismicity from the ISC Bulletin (International Seismological Centre, 2022, see section 3.2.1), and active fault traces. We will focus on the four sub-regions marked by blue boxes in Figure 1, due to their contrasting tectonic environments, represented by a heterogeneous spatial distribution of crustal seismicity and by the diversity of allochthonous terranes that have been accreted to the NW margin of South America (see Montes et al., 2019).

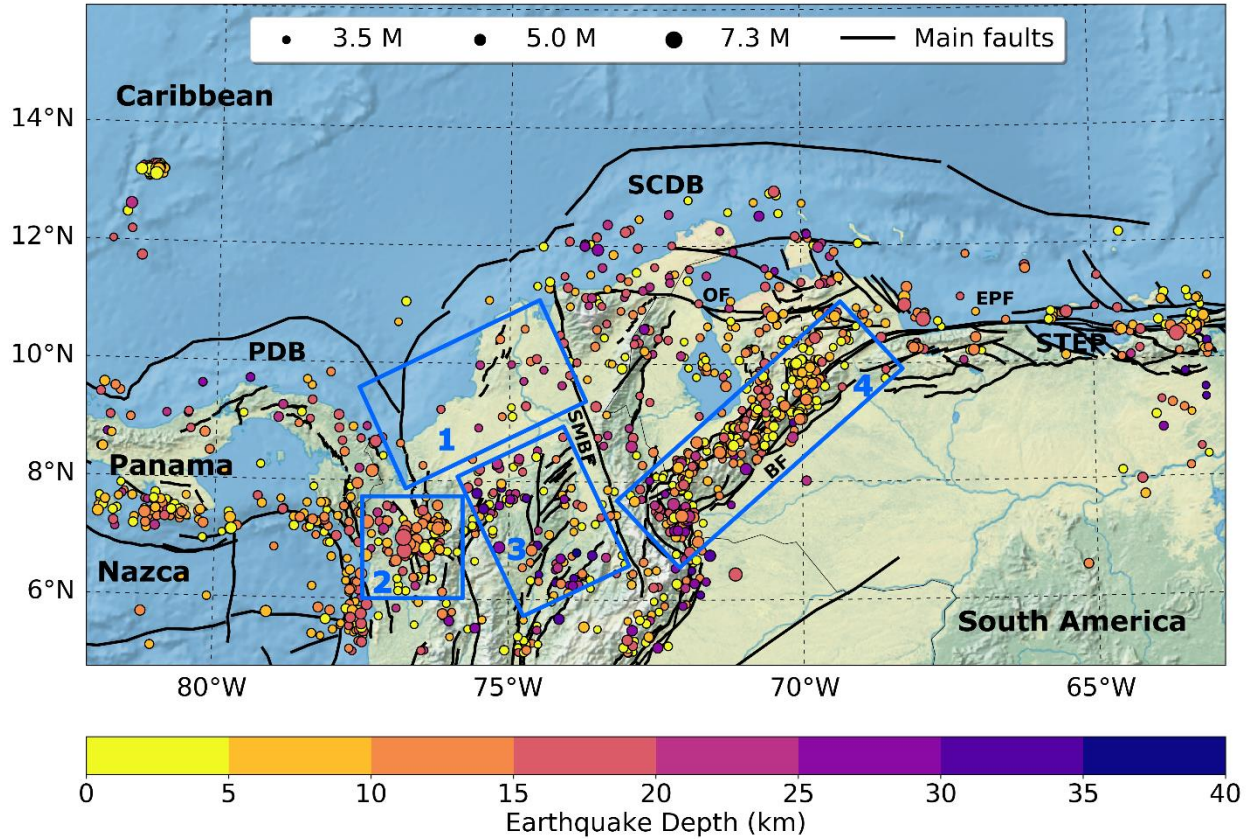


Figure 1. Crustal earthquakes with the best determined hypocentral depths in the region, selected from the ISC Bulletin (International Seismological Centre, 2022) as detailed in Sec. 3.2.1. Blue boxes: Sub-regions discussed in the main text. Black lines: Active fault traces as compiled by Styron et al. (2020) and Veloza et al. (2012). PDB = Panama deformed belt, SCDB = South Caribbean Deformed Belt and STEP = Subduction-Transform-Edge-Propagator fault system. Main fault systems are: BF = Boconó Fault, SMBF = Santa Marta - Bucaramanga Fault, EPF = El Pilar Fault, and OF = Oca-Ancon Fault.

Region 1 includes the Sinú-San Jacinto and Lower Magdalena basins, which correspond to important depocenters in the study area (Figure S1) with up to ~7 km of sedimentary cover (Laske et al., 2013). Both basins are crosscut by a northward continuation of the Romeral Fault system (RFS, Figure 3), which is interpreted as the paleo-suture between continental basement rocks to the east and oceanic basement rocks towards the west of the fault (Montes et al., 2019; Mora et al., 2017). Here the crustal seismicity is scarce and preferentially occurs at depths < 25 km.

Region 2 corresponds to the area around the Murindó seismic nest. In this region, the Uramita fault system (UF, Figure 3) acts as the suture between the (mainly) oceanic terranes of the western Cordillera, and the Panamá-Chocó block, dominated by plateau and magmatic arc terranes (Montes et al., 2019; Mosquera-Machado et al., 2009). Diverse active faults have been described in this area, including the Atrato, Mutatá and Murindó systems (MF, Figure 3). The latter has been considered responsible for the disastrous $M_s = 6.8$ foreshock and $M_s = 7.3$ mainshock

events, on 17th and 18th October 1992 (Mosquera-Machado et al., 2009), the largest earthquakes recorded in the study region since 1980. The mainshock caused widespread liquefaction, landslides, complete destruction of the center of Murindó town and even building damages and fatalities in Medellín, a city located more than 130 km away from the earthquake epicenter (Mosquera-Machado et al., 2009; Martínez et al., 1994). This region is characterized by a dense occurrence of earthquakes at intermediate crustal depths.

Region 3 includes the Otú, Palestina and El Espíritu Santo faults systems (Paris et al., 2000). The Palestina fault is a NE-SW strike-slip, right-lateral system that cuts the Central Cordillera and its formation may have been associated to the oblique subduction of the oceanic lithosphere during Late Cretaceous (Acosta et al., 2007). This system can be interpreted as the northward continuation of the large-scale brittle suture between the para-autochthonous terrane of NW South America and the allochthonous terrane of North Andes terranes (Kennan and Pindell, 2009). In this study, we grouped the Palestina and Otú-Pericos faults in what we will refer to as the Otú-Palestina fault system (OPF, Figure 3), even though those two structures might be genetically different (Restrepo & Toussaint, 1988). The right-lateral Espíritu Santo fault (ES, Figure 3) can be considered a part of the large-scale suture zone defined by the Romeral Fault System (Noriega-Londoño et al., 2020). This region concentrates most of the deepest seismic events of the study area.

Region 4 comprises the Venezuelan Andes, which includes the NE-SW Boconó fault system. This active fault network accommodates most of the Maracaibo block displacement with a right-lateral strike-slip motion, and serves as its boundary with South America (Pousse-Beltran et al., 2018 and references therein). The seismicity is deeper in the SW portion of the fault system and shows a smooth shallowing transition towards the NE.

3 Methods

3.1 Steady-state 3D thermal model and input data

The main mechanism of heat transport within the lithosphere is thermal conduction. In the crystalline crust, a first-order calculation can be obtained by a steady-state approach (Turcotte & Schubert, 2002), describe by the following equation:

$$H = \nabla(\lambda_b \nabla T) \quad \text{Eq. (1)}$$

where H is the radiogenic heat production, ∇ is the nabla operator, and λ_b the bulk thermal conductivity. The steady-state 3D thermal field is computed using a numerical model scheme based on the finite element method with the software GOLEM (Cacace & Jacquey, 2017). We used the uppermost 75 km of the gravity-constrained structural and density model by Gómez-García et al. (2020, 2021) as the main input with lithology-dependent thermal properties. In this steady-state assumption, the heat transport within the lithosphere depends on the temperatures used as boundary conditions and on the thermal properties of each lithospheric layer, i.e.: the radiogenic

heat production and the thermal conductivity (λ). Therefore, specific values were assigned to the different layers of the lithospheric model, as explained hereafter.

3.1.1 Lithospheric structural model and definition of thermal properties

The gravity-constrained structural and density model of the South Caribbean margin (details in Gómez-García et al., 2020, 2021) represents the complexity of the Caribbean realms by including fifteen different layers (**Table 1**). Aiming to have a detailed spatial resolution for the thermal calculations, the structural model was here refined to a 5 km x 5 km cell size.

The density of each layer, as constrained by 3D gravity modelling (Gómez-García et al., 2021) provides insights about its main lithology, and in turn, to thermal properties such as thermal conductivity and radiogenic heat production (e.g.: Ehlers, 2005; Hasterok et al., 2018; Vilà et al., 2010). Table 1 summarizes the lithologies inferred for each layer (which are compatible with derived densities and the geologic and tectonic setting of the Caribbean), the thermal properties used for the modelling, and the rationale of each choice. The supplementary material contains further details on how the thermal conductivities and radiogenic heat production were determined.

3.1.2 Upper and lower boundary conditions

The upper boundary condition (Figure 2a) for the thermal model is derived by integrating the average onshore surface temperatures from the ERA5-Land dataset, from January 2015 to April 2019 (Muñoz Sabater, 2019), and the average temperatures at the seafloor from GLORYS reanalysis for the year 2015 (Ferry et al., 2010). The integrated temperature field ranges from $\sim 1^\circ\text{C}$ in the portion of the Pacific Ocean that is included in the modelled domain, and reaches a maximum of $\sim 30^\circ\text{C}$ over Venezuelan territory. As expected, the temperatures over the mountains are the lowest of the continental realm, with an average of $\sim 8^\circ\text{C}$ for the period used in this research.

The temperature at 75 km depth was defined as the lower boundary condition (**Figure 2b**), which was calculated from a conversion of the S-wave velocities from the SL2013sv tomographic model (Schaeffer & Lebedev, 2013), following the approaches of Goes et al. (2000) and Meeßen (2017) and the composition shown in Table S1. This thermal boundary depicts two cold domains: the Guyana shield, with minimum temperatures of $\sim 912^\circ\text{C}$, and within the Caribbean region, with a mean value of $\sim 972^\circ\text{C}$. In contrasts, temperatures in the region where the Nazca and Caribbean slabs are present are higher than the surroundings, reaching up to $\sim 1100^\circ\text{C}$.

214 **Table 1.** Thermal properties defined for each lithospheric layer. Densities from Gómez-García et al. (2021). RHP: Radiogenic heat
 215 production. C-LIP: Caribbean Large Igneous Plateau. See details in the supplementary materials.

Layer	Density (kg m ⁻³)	Thermal conductivity (W m ⁻¹ K ⁻¹)	RHP (μ W m ⁻³)	Rationale for thermal conductivity	Reference for RHP
Oceanic sediments	2350	2.55	1.1	Average between sandstone, limestone and shale ^a	Mean value for sedimentary rocks ^b
Continental sediments	2500	3.5	1.19	Assuming sandstones ^a	Mean value for detritic sedimentary rocks ^b
Oceanic upper crust	3000	2.1	0.358	Mean value for basalts ^a	Mean value for basalts ^b
Low density bodies (Aves Ridge)	2900	2.6	1.07	Average for basalts and granites ^a following the composition by ^c	Eq. S1, using the average concentration of U, Th and K for Aves Ridge samples ^c
High density bodies in the upper oceanic crust	3250	2.93	0.057	Average for basalts, gabbros and peridotites ^a assuming a C-LIP mixed composition	Eq. S1, using the average concentration of U, Th and K for C-LIP samples ^d
Oceanic lower crust	3100	2.95	0.468	Mean value for gabbros ^a	Mean value for gabbros ^b

Low density bodies in the lower oceanic crust (Aves Ridge)	3000	2.6	1.07	Average for basalts and granites ^a following the composition by ^c	Eq. S1, using the average concentration of U, Th and K for Aves Ridge samples ^c
High density bodies in the lower oceanic crust	3250	2.93	0.057	Average for basalts, gabbros and peridotites ^a assuming a C-LIP mixed composition	Eq. S1, using the average concentration of U, Th and K for C-LIP samples ^d
Continental upper crust	2750	2.4	0.6	Assuming a granitic composition ^a	Assuming a granitic composition ^b
Low density bodies in the upper continental crust	2600 - 2650	2.1	0.4	Assuming a basaltic composition ^a	Assuming a basaltic composition ^b
High density body in the upper continental crust (Santa Marta massif)	3000	2.95	0.667	Mean value for gabbros ^a assuming a magmatic composition ^e	Assuming a gabbroic composition ^b
Continental lower crust	3070	2.4	0.5	Assuming a granitic composition ^a	Assuming a granitic composition ^b
High density subcrustal bodies	3242	4.15	0.01	Mean value for dunites ^a assuming a depleted,	Value for depleted peridotites ^b

				high-density mantle material	
Slab	3163	3.3	0.001	Assuming a prevalence of peridotites ^a	Eq. S1, using the average concentration of U, Th and K reported for depleted mantle ^a
Lithospheric mantle	3D solution	3	0.012	Assuming a peridotitic composition ^a	Eq. S1, using the average concentration of U, Th and K reported for mantle ^a

216 ^aTurcotte & Schubert (2002). ^bVilà et al. (2010). ^cNeill et al. (2011). ^dKerr (2014). ^eMontes et al. (2019).

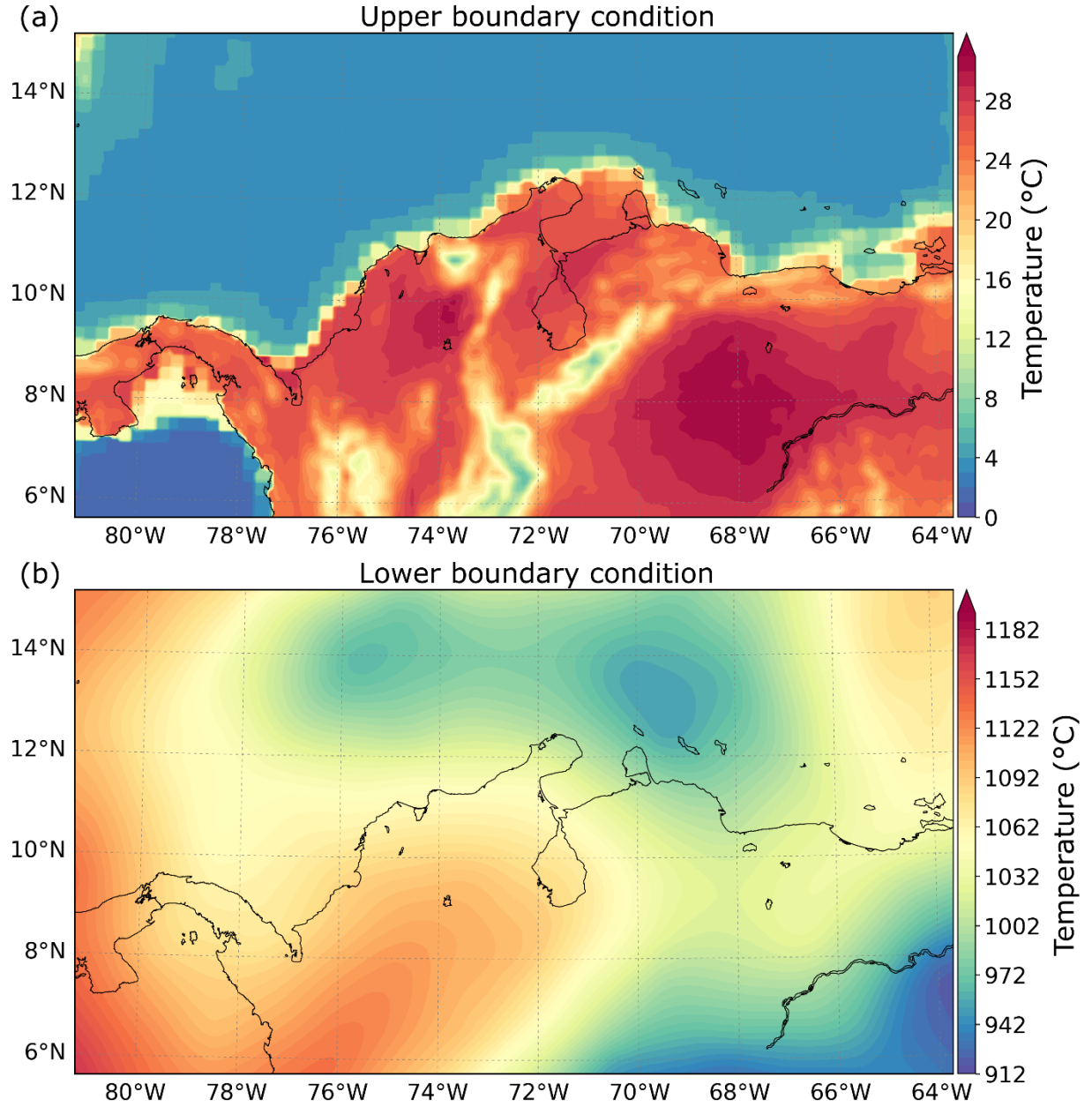


Figure 2. Boundary conditions assumed on the 3D steady-state thermal model. (a) Upper boundary integrating temperatures over the continent from the ERA5-Land dataset (Muñoz Sabater, 2019), and at the seabed from the GLORYS dataset (Ferry et al., 2010). (b) Lower boundary condition set as the temperatures at 75 km depth.

3.1.3 Validation of the modelled temperatures

The calculated 3D thermal field was validated by comparing measurements available from downhole temperatures (ANH, 2020) and surface heat flow (Lucazeau, 2019) with the

corresponding modelled values. Control point locations are shown in Figure 3. Only the heat flow observations with the highest qualities (error range between 10% and 20%) were considered. In general, the measured heat flow is lower within the Caribbean Sea (40-80 mW m⁻²) than in the Pacific Ocean (>80 mW m⁻²). The minimum values (10-40 mW m⁻²) are found close to the area of influence of the Magdalena Fan depocenter (MFD, Figure 3), likely as a result of thermal blanketing by the thick sedimentary sequence (Scheck-Wenderoth & Maystrenko, 2013).

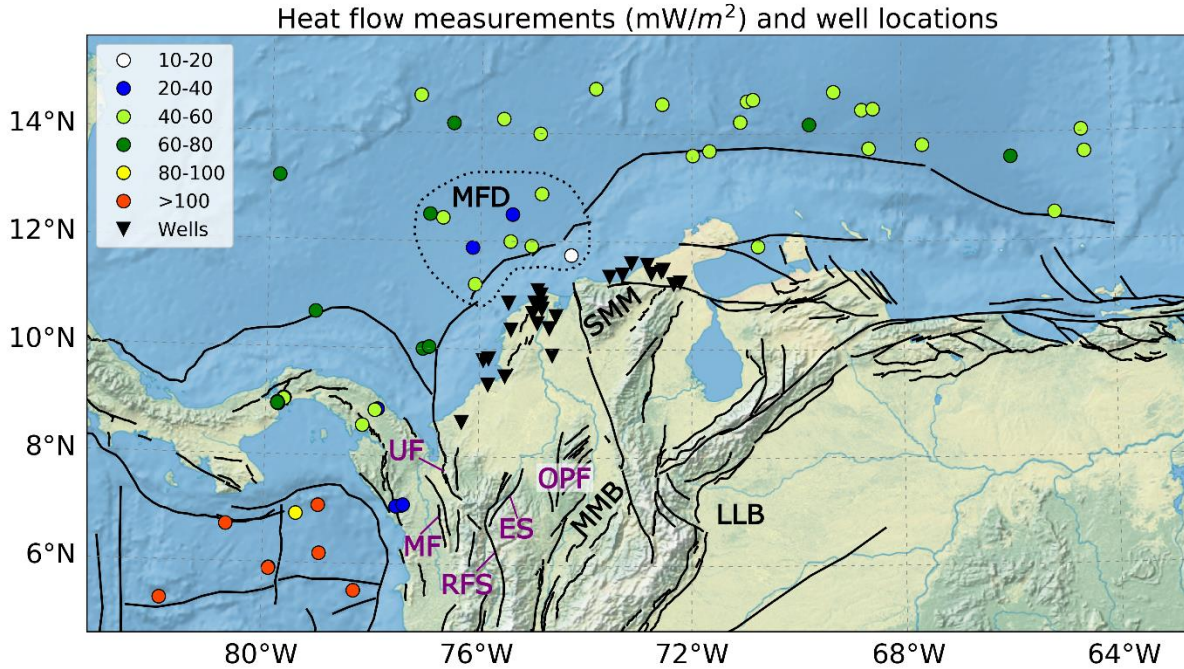


Figure 3. Measurements used for validating the thermal model. Color-coded dots: heat flow measurements with the highest qualities (Lucazeau, 2019). Black triangles: wells from the oil industry with measured downhole temperatures (ANH, 2020). Active fault traces (black lines) as in Figure 1. ES = Espiritu Santo Fault. OPF = Otú-Palestina Fault system. RFS = Romeral Fault System. MF = Murindó Fault. UF = Uramita Fault. Dotted polygon highlights the heat flow measurements close to the Magdalena Fan depocenter (MFD). Additional features discussed in the text: LLB = Llanos Basin. MMB = Middle Magdalena Basin. SMM = Santa Marta Massif.

3.2 Crustal seismogenic thickness

The depths of the upper and lower stability transitions for seismogenesis, and their difference (the crustal seismogenic thickness) were calculated from an earthquake catalog, as described below.

3.2.1 Earthquake catalog

Since the study area covers several countries, a global earthquake catalog was preferred over national ones. We therefore relied upon the reviewed ISC Bulletin (International

Seismological Centre, 2022), regarded as the definitive record of the Earth's seismicity. This catalogue has been completely rebuilt for the period 1964-2010 (Storchak et al., 2020), adding additional earthquakes and relocating hypocenters with the same location procedures used from 2011 onwards (Bondár & Storchak, 2011). However, for earthquakes occurring before 1980, the ISC Bulletin is still particularly heterogeneous (e.g.: Woessner & Wiemer, 2005). Therefore, we limit our study to the years following 1980. Only prime hypocentres (i.e.: those relocated, or considered as best determined by ISC, see Di Giacomo & Storchak, 2016) were used. At the time of writing, the bulletin has been reviewed until March 2020.

The ISC Bulletin frequently reports several magnitudes for each event. We chose only those associated with the prime hypocenter, and adopted the hierarchy proposed by ISC for selecting the most reliable, preferred magnitude type (Di Giacomo & Storchak, 2016) (see supplementary material). Earthquakes without reported magnitudes were disregarded. **Figure 4** shows the scatterplot of magnitude versus time for shallow earthquakes (with hypocentral depths ≤ 50 km, including all crustal seismicity) in the study area, which is useful for identifying heterogeneities and different periods in the compilation of the earthquake catalog (e.g.: Gentili et al., 2011; González, 2017).

A first quality threshold is the magnitude of completeness (M_c), below which not all earthquakes were recorded. Figure 4 shows that, in the study area, very few earthquakes with magnitude <4.0 were recorded before 1991, indicating an incompleteness at least below this value for that period. Earthquakes with magnitudes <3.5 have been recorded only irregularly, and more frequently since June 1993, when the Colombian national seismic network started to compile its earthquake catalog (Arcila et al., 2020). We choose this year for separating the whole catalogue in two periods, which we then use to determine M_c , using the maximum curvature method (Wiemer & Wyss, 2000) with its standard deviation calculated by bootstrap (Efron, 1979) with 1000 samples (following Woessner & Wiemer, 2005). In the first period (January 1980 - May 1993), $M_c = 4.6 \pm 0.2$; in the second one (June 1993 – March 2020), $M_c = 3.5 \pm 0.02$. Those mean M_c values represent the minimum magnitude thresholds considered in the subsequent analysis.

Earthquakes with non- reported depths, as well as those with depths reported as 0 km or fixed, or with reported depth error > 30 km were excluded from the analysis of hypocentral temperature determinations. This selection allowed pruning the worst located earthquakes but preserving a sufficient number of events to perform our analysis. Note that the hypocentral depth errors reported in the ISC Bulletin format are wide, since they cover the 90% uncertainty range (Biegalski et al., 1999). The possible impact of the remaining hypocentral depth uncertainties on the results will be commented on later.

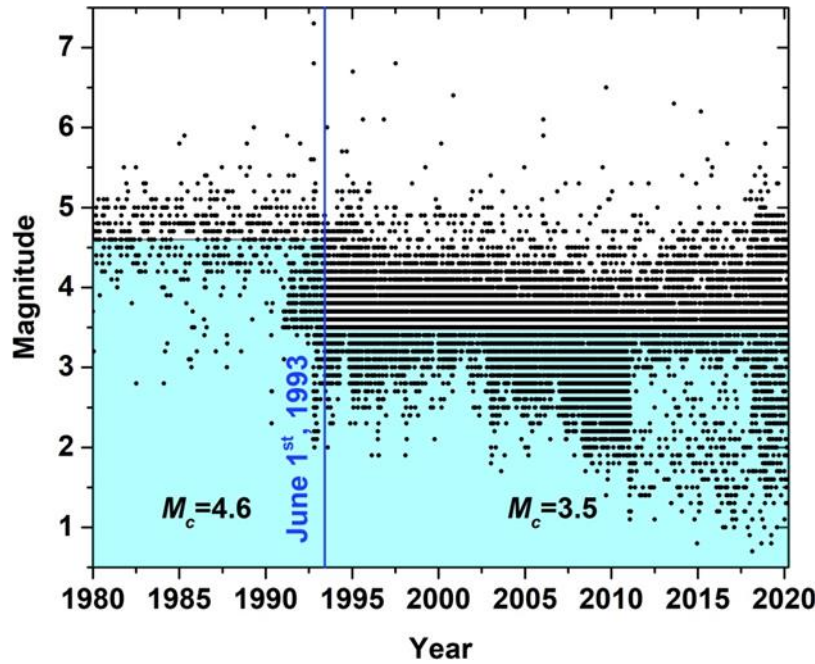


Figure 4. Magnitude versus time of earthquakes with depth ≤ 50 km in the study area, reported in the reviewed ISC Bulletin (International Seismological Centre, 2022). The vertical blue line marks the date at which the national seismic network of Colombia started operating, and separates two periods with different magnitude of completeness (M_c).

The reference surface used as depth=0 in the ISC Bulletin is the WGS84 reference ellipsoid (István Bóndar & Dimitri Storchak, pers. comm., 2020; see also Bondár & Storchak, 2011). Our thermal model considers the actual depth below sea level as reference, so hypocentral depths were referred to the EGM2008-5 geoid model (Pavlis et al., 2012). After this correction, earthquakes located above the solid Earth's surface (within the ocean water column or the atmosphere, according to the GEBCO topographic model, Weatherall et al., 2015) were excluded from our analysis. Such mislocations are the unfortunate consequence of disregarding the actual Earth's topography and bathymetry in the majority of the routine hypocentral depth determinations by ISC (and most seismological agencies). This location problem is emphasized in study areas such as ours, with several kilometers of topographic relief between the ocean bottom and the mountain tops.

Since we focus our analysis on crustal seismicity, we also disregarded earthquakes located below the crustal-to-mantle (Moho) boundary, as provided by the GEMMA model (Reguzzoni & Sampietro, 2015), interpolated to a homogeneous grid of $5 \text{ km} \times 5 \text{ km}$. We preferred the GEMMA model over other Moho depths available in the region (e.g.: Avellaneda-Jiménez et al., 2022; Poveda et al., 2018) because either these studies do not cover the entire study area, or portray large regions with data gaps, as they relied on available seismic stations. The remaining subset thus only contains the best located, crustal earthquakes in the region (Figure 1), which will be the ones used for calculating the upper and lower stability transitions (Section 3.2.2) and hypocentral temperatures (Section 4.2).

The scalar seismic moment (M_0 , in N·m) was calculated for this subset, from the standard IASPEI formula for the moment magnitude M_w (see Bormann, 2015 after Kanamori, 1977). If the preferred magnitude from the ISC Bulletin was not already M_w , it was first converted to it using the relations by Di Giacomo et al. (2015, exponential versions, for body-wave or surface-wave magnitudes), Arcila et al. (2020, for local magnitudes) and (Salazar et al., 2013, for duration magnitudes). The data repository (Gomez-Garcia et al., 2022) provides the analyzed earthquake subset, with their preferred magnitudes, estimated M_0 and calculated hypocentral temperatures.

3.2.2 Upper and lower stability transitions and uncertainty quantification

The 10% and 90% depth percentiles (D10 and D90, respectively; Marone & Scholz, 1988; Sibson, 1982) were spatially mapped considering the subset of crustal earthquakes with the best hypocentral depth determinations (see previous section). We used the median-unbiased percentile estimator of Hyndman & Fan (1996) at each node of a latitude-longitude grid with a spacing of 0.1° , considering the 20 closest earthquakes to each node as the sample for calculating the corresponding D10 and D90 values, provided that these events were at a maximum distance of 150 km from the node. To avoid boundary effects, we considered earthquakes outside the study area, applying the same selection procedure, after checking that M_c was not larger in this extended region (with a buffer of 150 km).

Whether this way of spatial sampling of a fixed number of the closest earthquakes is novel for calculating hypocentral depth percentiles, it has been frequently used for mapping M_c and b -values of the Gutenberg-Richter distribution (firstly by Wiemer & Wyss, 1997). The reason for our choice stems from the fact that it maximizes the mapping detail, that is, the resolution radius (epicentral distance to the 20th closest earthquake from the node in our case) will be small in locations with high spatial earthquake density, and large in locations with sparse seismicity. The upper threshold of this radius was chosen by inspection of the resulting maps, to avoid calculating D10 and D90 in regions where the spatial density of epicentres was too low to obtain reliable results. Further details of the resulting map resolution will be commented on in Section 4.4.

For each node, 10000 random bootstrap samples (Efron, 1979) were generated out of the corresponding 20 best estimates of the hypocentral depth values, and from them the average D10 and D90 values and their respective bootstrap standard deviations were calculated. Considering all nodes with percentile determinations, the mean standard deviation was 0.4 and 0.8 km, and the maximum one was 2.3 and 4.3 km, for D10 and D90 respectively (see histogram of standard deviations in Figure S2). These low uncertainties indicate that using 20 earthquakes for each node is already reliable in our case to obtain stable D10 and D90 values. Using a larger earthquake sample for each node was avoided, as it would imply enlarging the resolution radius, considering earthquakes located further away from the nodes, and thus smoothing out the spatial variations of D10 and D90.

The temperatures at the depths of D10 and D90 at each node of the map were calculated from the 3D thermal model. Due to the sampling method used for determining D10 and D90, in most nodes of the map the calculated D10 and D90 lie within the crust, but there are some in which the percentiles may be located above or below the crust, respectively. In either case, those nodes

lying outside the bounds of our structural model were not considered. The resulting D10 and D90 values, and their corresponding standard deviations are provided in the data repository (Gomez-Garcia et al., 2022).

4 Results and discussion

4.1 Model validation

In Figure 5a we compare the modelled and measured temperatures at different boreholes. Since no additional information was provided regarding the error of the measurements, the industry standard correction of increasing by a 10% the observations was applied to the original values (ANH, 2020). In general, there is a good correlation between the modelled temperatures (cyan dots) and the corrected values (black dots). The histogram of residuals (Figure 5a, right) indicates that most of the misfits range between -10 and 10°C, with a mean of -4.99°C; although larger misfits occur at shallower depths (< 1km). Such a trend could be explained by shallow advective processes of heat transport (e.g., by groundwater), which have not been considered in our model.

The modelled heat flow is generally lower than the measurements, except in the area of influence of the Magdalena Fan (Figure 5b). The heat flow data in the Pacific Ocean are located in an area of intense faulting (Marcaillou et al., 2006), close to the Panama Fracture Zone; therefore, additional advective heat transport might be responsible for the higher measured heat flow values in this region. Considering that the associated error in the heat flow data used in this analysis ranges between 10 and 20% (Lucazeau, 2019), it is possible to conclude that the model fits the regional trend, except in those two areas previously mentioned. Nevertheless, the heat flow data is usually affected by nonconductive processes, such as hydrothermal circulation. For this reason, their interpretation in terms of a purely conductive, lithospheric-scale model is difficult, as other authors have suggested (Klitzke et al., 2016; Scheck-Wenderoth & Maystrenko, 2013).

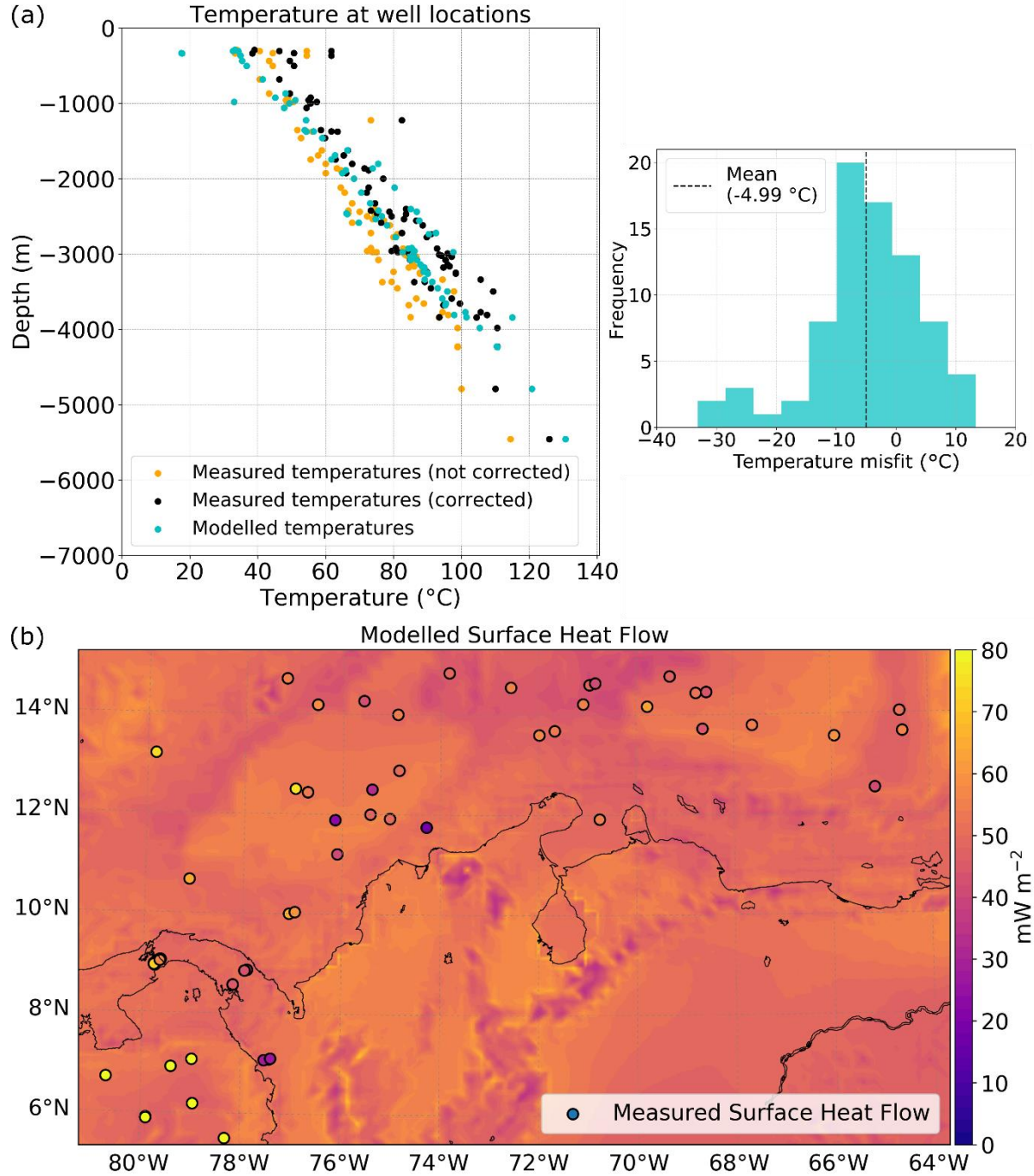


Figure 5. Validation of the 3D thermal field against measurements of downhole temperatures and surface heat flow. (a) Modelled temperatures show a good fit to the observed (corrected) temperatures. The largest misfits (histogram of the right panel) occur at depths shallower than 1km. (b) Calculated surface heat flow (background) and measured values (colored dots, with the same color bar).

4.2 Relation between lithology, hypocentral temperature and seismic moment release

The modelled hypocentral temperature distribution of the selected earthquake dataset is shown in **Figure 6**. We will focus our discussion in the four sub-regions previously defined in Figure 1.

The Sinú-San Jacinto and Lower Magdalena basins (region 1) are characterized by a scarce seismicity, especially compared to the surrounding North Andes terranes. The few recorded earthquakes seem to be broadly distributed at depth, which explains the variability in modelled hypocentral temperatures in this region. Seismicity is frequent in region 2, as it hosts the Murindó cluster, including the largest earthquake of the selected dataset ($M_s = 7.3$), with a hypocentral depth of 16.7 km (Figure 1), and an associated modelled temperature of $\sim 375^\circ\text{C}$. In the Otú-Palestina and El Espíritu Santo fault systems (region 3) the deepest hypocentral depths are reported (> 30 km) (Figure 1), giving as a result modelled hypocentral temperatures of more than 600°C . In the Venezuelan Andes, bounded by the Boconó fault (region 4) seismicity is denser than in the rest of the North Andes terranes, and shows a shallowing pattern from the southwest towards the northeast (Figure 2). Such a trend implies a transition from hotter hypocentral temperatures close to the Colombian-Venezuelan border towards colder ones in the Falcon basin.

A synthesis of modelled temperatures for the entire study area is presented in Figure 7. Figure 7b also depicts the seismogenic window typically associated with granite ($90\text{--}350^\circ\text{C}$), gabbro ($200\text{--}600^\circ\text{C}$) and olivine gouge ($600\text{--}1000^\circ\text{C}$), according to the review presented by Scholz (2019). Due to the large abundance of granitic rocks in continental realms, they usually are considered as good proxies for the seismogenesis in these crustal regions. However, the study area has a variety of allochthonous terranes that have attached to the margin, including large ophiolite sequences -associated to oceanic plateaus-, and magmatic arcs (Montes et al., 2019); therefore, the seismogenic windows of gabbro and olivine were also considered.

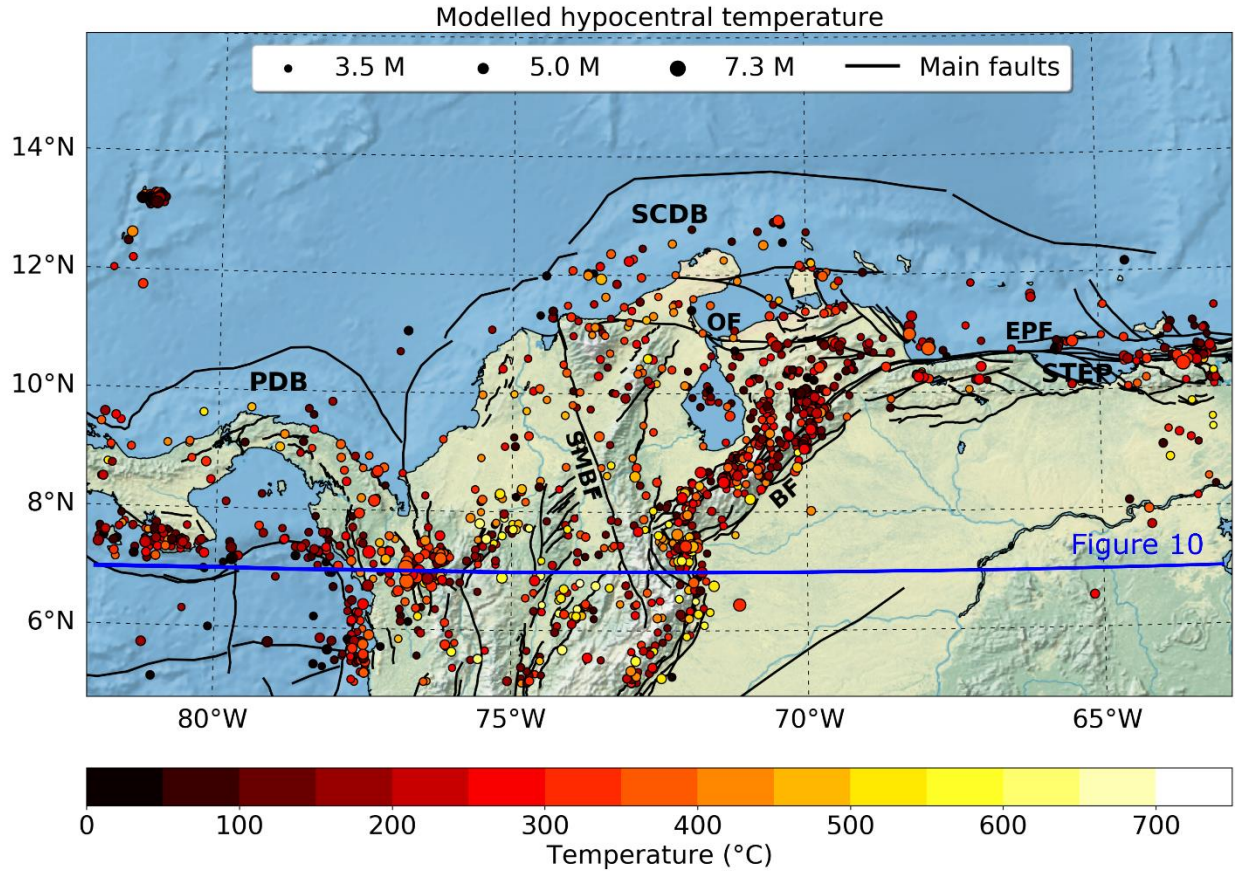


Figure 6. Modelled hypocentral temperature for crustal earthquakes. Acronyms and active fault traces (black lines) as in Figure 1. The surface projection of the vertical profile of Figure 10 is shown as a blue line.

The majority of the seismic events share hypocentral temperatures of less than 350°C (Figure 7a), within the observed seismogenic window of granite and partially overlaps with that of gabbro (Figure 7b). Nevertheless, modelled temperatures range from 1°C (offshore events) to almost 700°C, with only few events reaching the seismogenic window reported for olivine gouges at > 600°C. These ranges, however, are not strict because in nature rocks are a mix of different minerals that can contribute to a more complex behavior. For example, mixtures of 65% illite and 35% quartz might exhibit a seismogenic window between 250 and 400°C, while replacing the illite for muscovite implies a new window between 350 and 500°C (see grey dashed line in Figure 7b) (Scholz, 2019 and references therein).

The hypocentral depths show a bimodal distribution, with the largest peak between 0 and 5 km and a smaller one at ~10 km (Figure 7c). Computing D10 and D90 associated to the whole catalog of selected crustal earthquakes gives as a result a regional seismogenic zone ranging on average between 1.8 and 20.9 km. The occurrence of seismicity at very shallow depths (< 2km) suggest that no well-developed faults are also present in the study area (Scholz, 2019). However, despite of the detailed selection of the best located earthquakes (see section 3.2.1), large errors in

the hypocentral depths still remain (up to 30 km, see Figure S3), and should be considered in the analysis of our results.

The largest events ($M > 6.5$) were recorded between 15 km and 20 km depth (dark blue dots in Figure 7b), close to the lower stability transition (D90). This behavior supports early findings broadly debated in the literature (e.g.: Tse & Rice, 1986), and suggests that ruptures which initiated at deep high-stress regions are able to propagate through the entire seismogenic zone and probably reach the surface, resulting in a large rupture area, and therefore, in a large magnitude event. In particular, our analysis indicates that this could have occurred in the Murindó sequence in 1992. The two largest events ($M_s = 7.3$ and $M_s = 6.8$) occurred at the base of the seismogenic zone (16.7 km and 15.5 km, respectively), and are dominating the seismic energy liberation in the study area, as can be observed on the seismic moment release curve (Figure 7d). The geological effects of the 18 October 1992 mainshock evidence that it probably caused surface rupture exceeding 100 km in length (Mosquera-Machado et al., 2009), compatible with the overall rupture length deduced from the source-time functions of the earthquake sub-events (Li & Toksoz, 1993) and the size of the aftershock distribution (Arvidsson et al., 2002). Thus, we infer that the mainshock ruptured the whole seismogenic crust, from its base up to the surface.

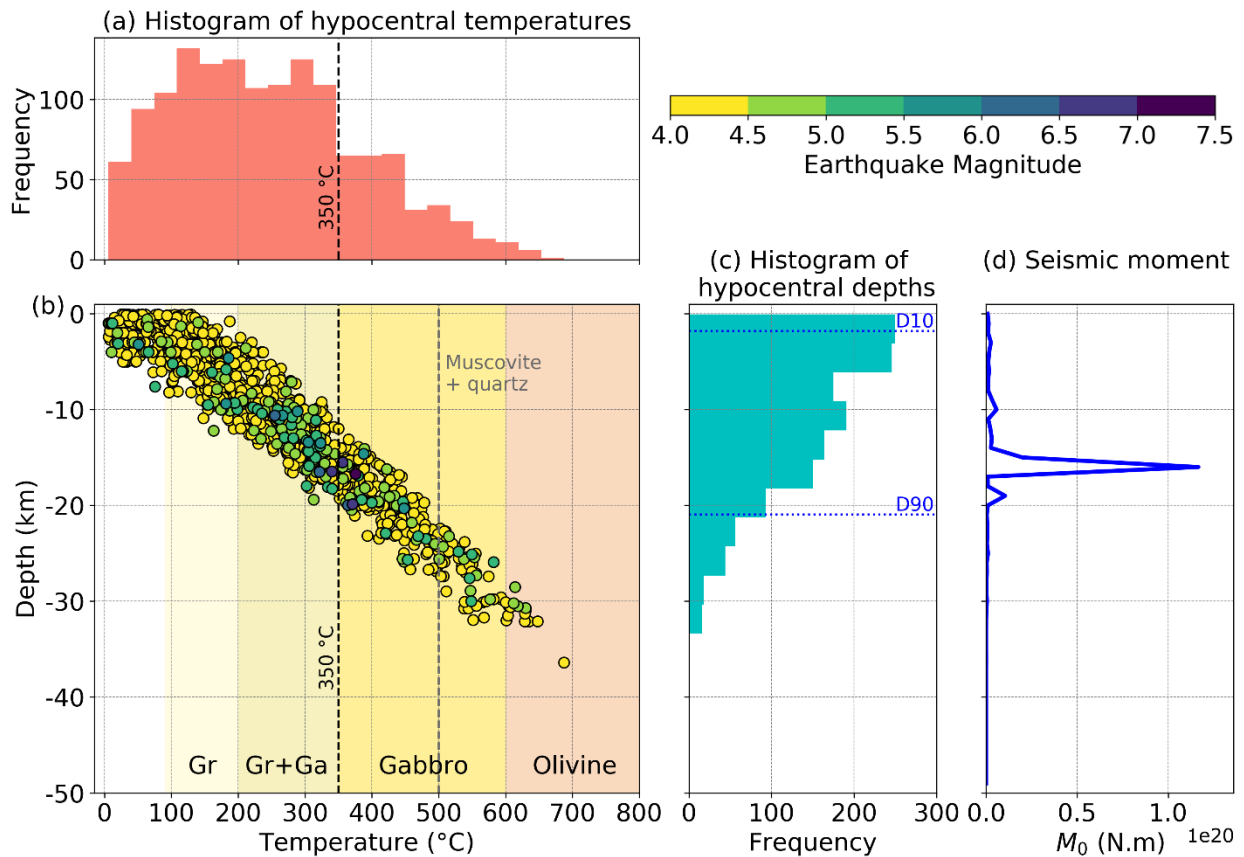


Figure 7. Synthesis of the modelled hypocentral temperatures. (a) Histogram of hypocentral temperatures. (b) Modelled temperature versus depth and preferred magnitude. Different colored

domains represent the seismogenic window of different rocks/minerals. Gr = Granite. Gr+Ga = shared seismogenic window between granite and gabbro. (c) Histogram of hypocentral depths with regional D10 = 1.8 km and D90 = 20.9 km. (d) Histogram of seismic moment release (M_0 , in N·m) as a function of depth, with depth bins of 1 km.

4.3 Depths and temperatures at the upper and lower stability transitions (D10 and D90)

In the Sinú-San Jacinto and Lower Magdalena valley (region 1) the depth to the upper stability transition (D10, Figure 8a) is relatively shallow (~1 to 2 km depth) and spatially homogeneous, since the few seismic events present in this region (Figure 6) do not allow resolving heterogeneities. Close to the Murindó nest (region 2), the Uramita fault acts as a preferential boundary between deeper D10 values in the Panamá-Chocó block, and shallower ones to the east of the fault, in the northern part of the Western Cordillera. In region 3, D10 reaches a local maximum of almost 10 km depth in the Otú-Palestina system. The Venezuelan Andes (region 4) are characterized by relatively homogeneous, shallow values of D10 of less than 2 km. The Oca-Ancon fault systems bound deep D10 values towards the north of the fault, and shallow values towards the south.

The most remarkable patterns found about the lower stability transition (D90, Figure 8b) are its deep values associated to the Otú-Palestina and El Espíritu Santo fault systems (region 3). D90 depths of almost 35 km in the Otú-Palestina are in agreement with the crustal-scale structure that these systems likely represent (Kennan & Pindell, 2009) and consistent with significant rheological contrasts in the transition between the Central and Eastern Cordilleras. The D90 values in the Venezuelan Andes are clearly bounded by the presence of major faults, reaching shallow depths of up to 8 km. However, the signal of the Uramita and Oca-Ancon faults acting as a boundary of terranes as previously discussed per the D10 is not present in the D90 map.

The temperatures along the D10 surface (Figure 8c) are highly influenced by a topographic effect. Their maximum values correlate spatially to elevated mountains in the Andes and the Santa Marta massif (SMM, Figure 3), with a few exceptions north of the Oca-Ancon fault. The temperatures along the D90 surface (Figure 8d), on the other hand, do not depict such strong correlation with topography. Instead, the hottest domains are associated to sedimentary basins (Figure S1) and correspond to the deepest values of D90, i.e.: underneath the Otú-Palestina and El Espíritu Santo fault systems (region 3), influenced by the Middle Magdalena basin (MMB, Figure 3), and beneath the Eastern Venezuelan and the Llanos basins (LLB, Figure 3).

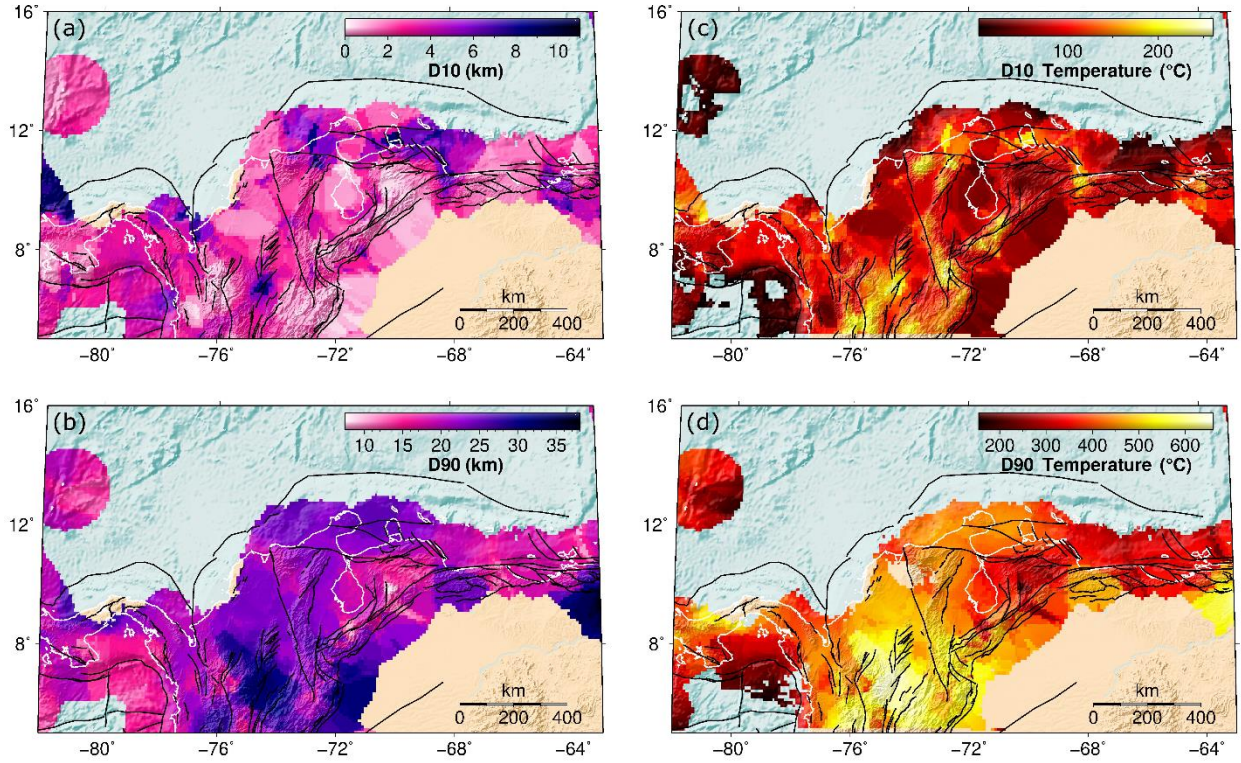


Figure 8. Depths and modelled temperatures of the upper (D10) and lower (D90) stability transitions for crustal seismicity. (a) D10. (b) D90. (c) D10 temperature. (d) D90 temperature. Black lines: active fault traces, as in Figure 1. Coastline depicted as white lines.

Our results suggest that the LST in the continental realm occurs at a wide range of temperatures, and in most of the study area, at values larger than those reported as the onset of quartz plasticity ($\sim 300^{\circ}\text{C}$, Zielke et al., 2020) or even larger than the temperature range at which brittle faulting in the crust is expected to cease ($350 \pm 100^{\circ}\text{C}$ – see a detailed review by Chen et al., 2013). The D90 temperatures are also higher than the seismogenic window of rocks and mineral assemblies typically found in continental crust (see Figure 7 and section 4.2).

Such behavior should be interpreted considering the following arguments: 1) there are still large uncertainties in the filtered events used in this study (up to 30 km) that could strongly influence the resulting D10 and D90 values; 2) the remaining earthquake dataset has a relatively small number of events, limiting the spatial resolution of the seismogenic thickness calculation (this is discussed in Section 4.4); 3) the dataset includes aftershocks, which may nucleate at depths larger than the base of the background seismogenic zone (e.g.: Zielke et al., 2020), so the calculated D90 values may be affected by transient deepening of the LST during aftershock sequences; 4) the diverse lithology of the allochthonous terranes accreted to NW South America includes ultramafic, olivine-rich rocks that are not typically forming continental crust, and therefore, could generate seismicity at temperatures larger than the seismogenic windows of granites and gabbros; 5) a thick lower crust together with a relatively hot upper mantle could contribute to large hypocentral temperatures (discussed in Section 4.4); and, 6) it is necessary to have more control points within

the continental region to constrain the thermal model, as there is a wide range of radiogenic heat production and thermal conductivity values that could potentially fit a particular lithology (e.g.: Vilà et al., 2010).

4.4 Crustal seismogenic thickness

The crustal seismogenic thickness shows large variations in the study area (Figure 9a). The minimum values (~7 km) are present in the Pacific Ocean offshore Panamá. A thin seismogenic crust is also observed along the Venezuelan Andes and offshore Venezuela, bounded by the Boconó and El Pilar fault systems. Higher seismogenic thicknesses (>30 km) are found in the Eastern Venezuelan basin and in the Otú-Palestina and El Espíritu Santo fault systems (region 3). We interpret the results in region 3 as indicating that the main faults in the area are well-developed crustal-scale structures, rather than shallow fault systems.

The reliability of these results (including both D10 and D90) highly depends on the density of earthquakes available for their calculation. This can be observed in the resolution radius map (Figure 9b), which shows the search radius required for reaching 20 seismic events in the calculation of D10 and D90. As we allowed a maximum radius of 150 km, the map is truncated at this value. It is possible to observe how regions with dense seismicity required a small radius for reaching the 20 events, including the Murindó nest (region 2) and the Venezuelan Andes (region 4). In contrast, the Sinú-San Jacinto and Lower Magdalena basins (region 1) are characterized by a rather low density of seismic events, reaching the maximum resolution radius allowed (150 km).

The sources of error in the calculation of the CST are diverse, and include uncertainties in the Moho depths, as well as errors in the hypocentral depths of earthquakes. The errors associated with the Moho depths (Figure S4) are large over the Nazca and South American realms, resulting in uncertainties about the location of the earthquakes either in the lithospheric mantle (including both the mantle wedge and the subducting slab), or in the lower continental crust.

Figure 10 shows a longitudinal profile along 7°N (see Figure 6 for spatial location). Here it is possible to observe the thermal response of the system, considering the spatially heterogeneous lower boundary condition at 75 km depth. In the Pacific Ocean, the 600°C isotherm bounds the majority of the seismic events located within the crust and uppermost mantle (black and grey dots), as previously suggested by Chen & Molnar (1983) and McKenzie et al. (2005), while the isotherm gradually shifts upward underneath western South America.

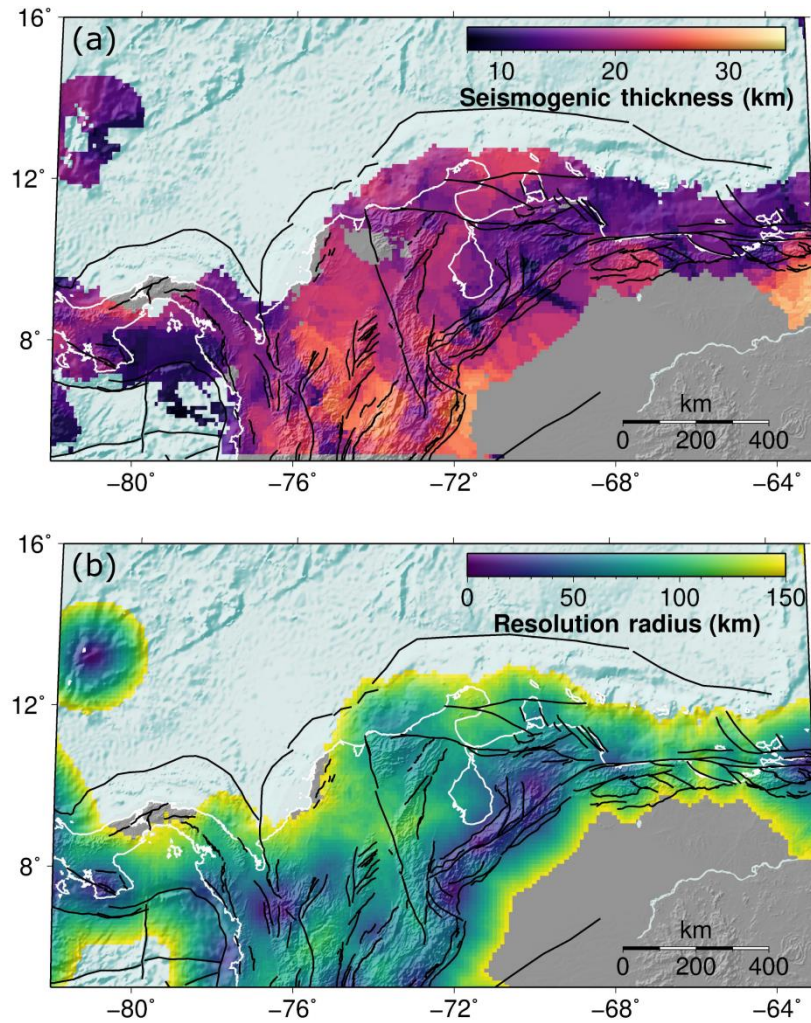


Figure 9. (a) Seismogenic thickness computed with the D10 and D90 values existing within the crust. (b) The resolution radius used to compute D10 and D90 shows high spatial variation and highlights regions with high and low density of seismic events. Black lines: active fault traces as in Figure 1.

The thermal structure of the continental realm is usually more complex than that of the oceanic lithosphere. However, the general agreement is that the colder (stronger) the lithosphere is, the deeper and higher magnitudes earthquakes it can host (e.g.: Chen et al., 2013). Our results suggest that the lithospheric mantle underneath the Colombian Andes is hotter than the surroundings, as indicated by a shallowing of the 600°C isotherm (Figure 10). As a response, most of the crustal seismicity there preferentially occurs at shallower depths. Nevertheless, deep events below the Moho interface (grey dots) are also present in this area, especially close to the Coiba slab. Considering the uncertainties in the hypocentral depths, and also in the Moho estimates from the GEMMA model (up to ~7 km along this profile, Reguzzoni & Sampietro, 2015) it is especially challenging to make a clear statement about these upper mantle events, but it is expected that the subducting Coiba plate can host such intraplate events. Similarly, the occurrence of upper mantle

earthquakes is nowadays broadly recognized (e.g.: Chen et al., 2013) as also dehydration reactions can trigger seismicity at temperatures above the normal BDT (e.g.: Rodríguez Picada et al., 2022).

Two regions with prominent seismic activity at a crustal scale are recognized: the suture of the Panamá-Chocó block with NW South America, around the Murindó nest; and close to the Guaicaramo and Yopal faults, the boundary between the North Andes terranes (Eastern cordillera) and the Guyana shield. As previously mentioned, most of the seismic activity in these areas is bounded by the 600°C isotherm. In these regions, the seismogenic thickness and the depths to the upper and lower stability transitions do not show any direct spatial correlation with variations in the Moho depth. However, the seismogenic crust is thicker and deeper where the largest depocenters are present, that is, the Middle Magdalena (MMB) and the Llanos basins (LLB).

In particular, the abrupt deepening of D90 between ~74°W and 76°W spatially correlates with a thick lower crust and with the shallowing of the 600°C isotherm, suggesting that a mafic crust able to host deeper earthquakes (deeper BDT) together with a hot upper mantle could contribute to the high hypocentral temperatures obtained in region 3, underneath the MMB.

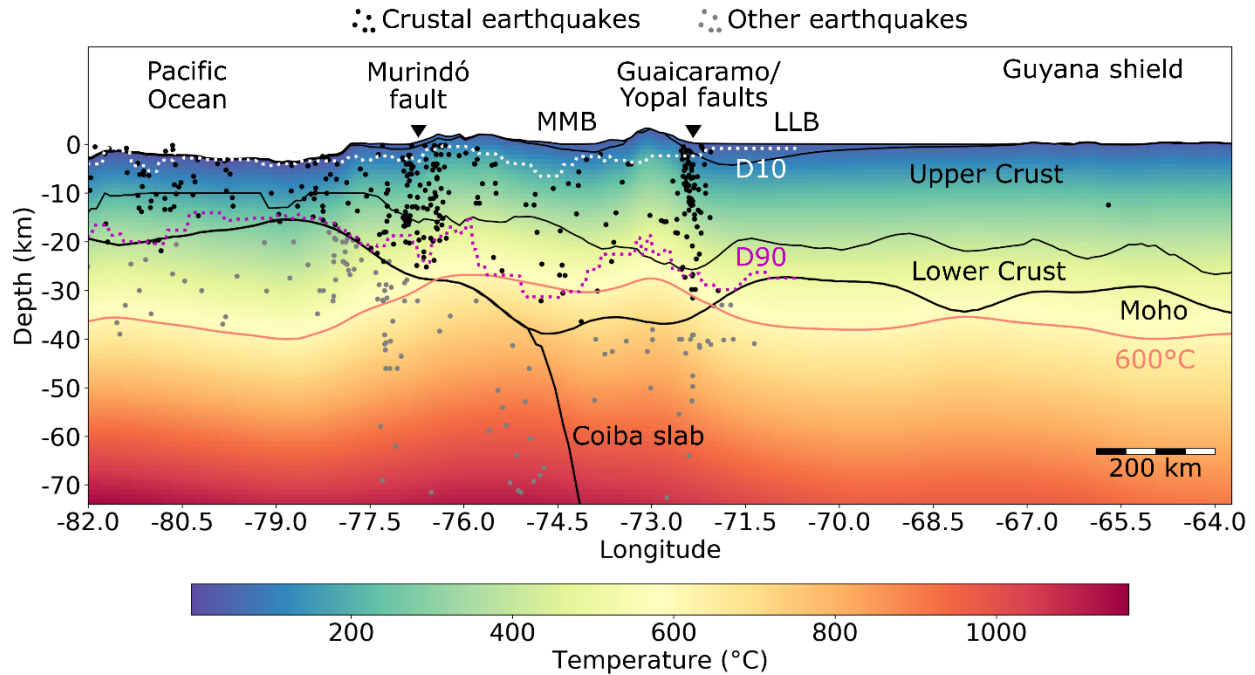


Figure 10. Profile at 7°N (see location in Figure 6) showing the modelled temperatures and their relation to the lithospheric structure (after Gómez-García et al., 2020, 2021), topography and seismicity. Vertical scale exaggerated. Pink continuous line: 600°C isotherm. Dotted lines: Depths to the upper and lower stability transitions (D10 and D90, respectively). Black lines: Boundaries of the lithospheric layers of the structural model. Black dots: Crustal earthquakes used in this study. Grey dots: Earthquakes deeper than the Moho interface, not used for calculating D10 or D90. The earthquakes projected in the profile include those from 6.5°N to 7.5°N. LLB = Llanos Basin. MMB = Middle Magdalena Basin (which spatially correspond with region 3).

560 5 Conclusions

561 We have calculated the depth to the upper (D10) and lower (D90) earthquake stability
 562 transitions, and the CST in NW South America, considering only crustal seismicity. This approach
 563 allows focusing on the seismogenic properties of the crust. Using a spatial sampling procedure
 564 depending on the spatial earthquake density, we were able to map variations of D10, D90 and the
 565 CST. Some of these variations are shown to correlate with crustal-scale faults in the region, which
 566 consequently separate crustal domains with different seismogenic behaviors. These calculations
 567 are limited by the completeness of the earthquake catalog, and the precision of the hypocentral
 568 locations. They could be eventually refined in future analyses, as new earthquakes are being
 569 recorded, particularly of smaller magnitudes than those considered here ($M < 3.5$).

570 Our three-dimensional approach for the calculation of the thermal field allows to retrieve
 571 spatial variations which would have been overlooked by simplified 1-D or 2-D models. Therefore,
 572 our workflow provides a good opportunity to compare limiting temperatures for seismogenesis
 573 provided by laboratory experiments against real-case scenarios, where the geological complexities
 574 are taken into account, including a realistic lithospheric structure and the mantle imprint into the
 575 crustal temperatures.

576 Most crustal seismic events in the study area have modelled hypocentral temperatures of
 577 less than 350°C, and are located at depths shallower than 20 km. Although most of the hypocentral
 578 temperatures range in the reported seismogenic window of rocks and mineral assemblies typically
 579 found in continental crust, some of the deepest hypocenters have associated temperatures $> 600^\circ\text{C}$,
 580 reaching the seismogenic window of olivine. This can be explained by either a thick, mafic lower
 581 crust, a hot upper mantle, large uncertainties of the Moho depths in the study area (up to 7 km), or
 582 by the still large errors associated to the hypocentral depths (up to 30 km), which could imply that
 583 those events actually occurred in the upper mantle. Alternatively, since diverse allochthonous
 584 crustal blocks have attached to the NW South American margin, including large ophiolite
 585 sequences, their composition may contain olivine-rich, ultramafic rocks able to host these
 586 earthquakes.

587 Our results evidence that the ruptures of the two largest events occurred in the region since
 588 1980 ($M_s = 6.8$ and $M_s = 7.3$), pertaining to the Murindó sequence of 1992, propagated from the
 589 base of the seismogenic zone (lower stability transition). This highlights the importance of
 590 considering this transition for defining the lower boundary of seismogenic sources in seismic
 591 hazard assessments.

592 The estimated seismogenic thickness in the Otú-Palestina and El Espíritu Santo fault
 593 systems is one of the largest in the study area (up to ~ 30 km), as the deepest events have been
 594 recorded in these regions. This suggests that these fault systems likely behave as crustal scale
 595 structures, which might have the potential of rupturing large areas, giving as a result large-
 596 magnitude, hazardous events.

Lastly, the seismogenic crust is thicker and hotter below the thick Middle Magdalena basin, suggesting that the thermal blanketing effect of the sedimentary cover may be able to affect the seismogenic behavior of the underlying crust.

Acknowledgments

AMGG was partially supported by grants from the German Academic Exchange Service (DAAD, 57314023 and 57440918), the Corporation Center of Excellence in Marine Sciences (CEMarin), Fundación para la Promoción de la Investigación y la Tecnología (Banco de la República de Colombia), the Centre de Recerca Matemàtica (CRM) in Barcelona, and the ESM-project of the Helmholtz Impulse and Networking Funds. ÁG is supported by the grants IJC2020-043372-I/AEI/10.13039/501100011033 (State Research Agency, AEI, from Spain) and PID2021-125979OB-I00 (MCIU/AEI/FEDER, UE). AMGG is grateful with Antoine Jacquey for his advice during early versions of the thermal models.

Open Research

The results of this publication are available in the data repository Gómez-García et al. (2022). The repository includes the calculated 3D thermal model, the filtered earthquake catalog with the modelled hypocentral temperatures, the seismic moment associated to each event, and the depths and temperatures of the upper and lower stability transitions (D10 and D90).

The thermal calculations were computed using the software GOLEM (Cacace & Jacquey, 2017) available at Jacquey & Cacace (2017). The figures were created using diverse Python packages (Python Software Foundation. Python Language Reference, version 2.7. Available at <http://www.python.org>) and GMT (Wessel & Smith, 1991).

References

- Acosta, J., Velandia, F., Osorio, J., Lonergan, L., & Mora, H. (2007). Strike-slip deformation within the Colombian Andes. *Geological Society Special Publication*, 272(January), 303–319. <https://doi.org/10.1144/GSL.SP.2007.272.01.16>
- ANH. (2020). Banco de información petrolera. Retrieved March 21, 2020, from [https://www.anh.gov.co/Banco de informacion petrolera/EPIS/Paginas/default.aspx](https://www.anh.gov.co/Banco%20de%20informacion%20petrolera/EPIS/Paginas/default.aspx)
- Arcila, M., García, J., Montejó, J., Eraso, J., Valcarcel, J., Mora, M., et al. (2020). Modelo nacional de amenaza sísmica para Colombia. Bogotá: Servicio Geológico Colombiano & Global Earthquake Model Foundation. DOI:10.32685/9789585279469.
- Arvidsson, R., Boutet, J. T., & Kulhanek, O. (2002). Foreshocks and aftershocks of the Mw=7.1 , 1992, earthquake in the Atrato region, Colombia. *Journal of Seismology*, 6, 1–11.
- Audemard, F. A. M. (1996). Paleoseismicity studies on the Oca-Ancón fault system, northwestern Venezuela. *Tectonophysics*, 259(1–3), 67–80. [https://doi.org/10.1016/0040-1951\(95\)00144-](https://doi.org/10.1016/0040-1951(95)00144-)

631 1

- 632 Avellaneda-Jiménez, D. S., Monsalve, G., León, S., & Gómez-García, A. M. (2022). Insights into
 633 Moho depth beneath the northwestern Andean region from gravity data inversion.
 634 *Geophysical Journal International*, 229(3), 1964–1977. <https://doi.org/10.1093/gji/ggac041>
- 635 Biegalski, K. F., Bohlin, J., Carter, J. A., Coyne, J., Dompierre, D., Novosel, G., & Rinehart, C.
 636 (1999). *Formats and protocols for messages – IMS1.0. International Data Center & Science*
 637 *Applications International Corporation. Document SAIC-99/3004.*
- 638 Bondár, I., & Storchak, D. (2011). Improved location procedures at the International Seismological
 639 Centre. *Geophysical Journal International*, 186(3), 1220–1244.
 640 <https://doi.org/10.1111/j.1365-246X.2011.05107.x>
- 641 Bormann, P. (2015). Are new data suggesting a revision of the current Mw and Me scaling
 642 formulas? *Journal of Seismology*, 19(4), 989–1002. [https://doi.org/10.1007/s10950-015-](https://doi.org/10.1007/s10950-015-9507-y)
 643 [9507-y](https://doi.org/10.1007/s10950-015-9507-y)
- 644 Cacace, M., & Jacquey, A. B. (2017). Flexible parallel implicit modelling of coupled thermal-
 645 hydraulic-mechanical processes in fractured rocks. *Solid Earth*, 8(5), 921–941.
 646 <https://doi.org/10.5194/se-8-921-2017>
- 647 Chen, W.-P., & Molnar, P. (1983). Focal depths of intracontinental and intraplate earthquakes and
 648 their implications for the thermal and mechanical properties of the lithosphere. *Journal of*
 649 *Geophysical Research*, 88(B5), 4183–4214. <https://doi.org/10.1029/jb088ib05p04183>
- 650 Chen, W. P., Yu, C. Q., Tseng, T. L., Yang, Z., Wang, C. yuen, Ning, J., & Leonard, T. (2013).
 651 Moho, seismogenesis, and rheology of the lithosphere. *Tectonophysics*, 609(January 2021),
 652 491–503. <https://doi.org/10.1016/j.tecto.2012.12.019>
- 653 Efron, B. (1979). Bootstrap methods: another look at the jackknife. *Annals of Statistics*, 7(1), 1–
 654 26.
- 655 Ehlers, T. A. (2005). Crustal thermal processes and the interpretation of thermochronometer data.
 656 *Reviews in Mineralogy and Geochemistry*, 58, 315–350.
 657 <https://doi.org/10.2138/rmg.2005.58.12>
- 658 Ferry, N., Parent, L., Garric, G., Barnier, B., & Jourdain, N. C. (2010). Mercator global Eddy
 659 permitting ocean reanalysis GLORYS1V1: Description and results. *Mercator-Ocean*
 660 *Quarterly Newsletter*, 34(January), 15–27.
- 661 Gentili, S., Sukan, M., Peruzza, L., & Schorlemmer, D. (2011). Probabilistic completeness
 662 assessment of the past 30 years of seismic monitoring in northeastern Italy. *Physics of the*
 663 *Earth and Planetary Interiors*, 186(1–2), 81–96. <https://doi.org/10.1016/j.pepi.2011.03.005>

- 664 Di Giacomo, D., & Storchak, D. A. (2016). A scheme to set preferred magnitudes in the ISC
665 Bulletin. *Journal of Seismology*, 20(2), 555–567. <https://doi.org/10.1007/s10950-015-9543-7>
- 666 Di Giacomo, D., Bondár, I., Storchak, D. A., Engdahl, E. R., Bormann, P., & Harris, J. (2015).
667 ISC-GEM: Global Instrumental Earthquake Catalogue (1900-2009), III. Re-computed MS
668 and mb, proxy MW, final magnitude composition and completeness assessment. *Physics of
669 the Earth and Planetary Interiors*, 239, 33–47. <https://doi.org/10.1016/j.pepi.2014.06.005>
- 670 Goes, S., Govers, R., & Vacher, P. (2000). Shallow mantle temperatures under Europe from P and
671 S wave tomography. *Journal Of Geophysical Research-Solid Earth*, 105(B5), 11153–11169.
672 <https://doi.org/10.1029/1999jb900300>
- 673 Gómez-García, Á. M., González, Á., Cacace, M., Scheck-Wenderoth, M., Monsalve, G. (2022).
674 Hypocentral temperatures, crustal seismogenic thickness and 3D thermal model of the South
675 Caribbean and NW South America. GFZ Data Services.
676 <https://doi.org/10.5880/GFZ.4.5.20202.005>.
- 677 Gómez-García, Á. M., Le Breton, E., Scheck-Wenderoth, M., Monsalve, G., & Anikiev, D. (2020).
678 3D lithospheric structure of the Caribbean and north South American Plates and Rotation
679 Files of Kinematic Reconstructions back to 90 Ma of the Caribbean Large Igneous Plateau.
680 <https://doi.org/https://doi.org/10.5880/GFZ.4.5.2020.003>
- 681 Gómez-García, Á. M., Le Breton, E., Scheck-Wenderoth, M., Monsalve, G., & Anikiev, D. (2021).
682 The preserved plume of the Caribbean Large Igneous Plateau revealed by 3D data-integrative
683 models. *Solid Earth*, 12(1), 275–298. <https://doi.org/10.5194/se-12-275-2021>
- 684 González, Á. (2017). The Spanish National Earthquake Catalogue: Evolution, precision and
685 completeness. *Journal of Seismology*, 21(3), 435–471. <https://doi.org/10.1007/s10950-016-9610-8>
686
- 687 Gutscher, M. A., Klingelhoefer, F., Theunissen, T., Spakman, W., Berthet, T., Wang, T. K., &
688 Lee, C. S. (2016). Thermal modeling of the SW Ryukyu forearc (Taiwan): Implications for
689 the seismogenic zone and the age of the subducting Philippine Sea Plate (Huatung Basin).
690 *Tectonophysics*, 692, 131–142. <https://doi.org/10.1016/j.tecto.2016.03.029>
- 691 Hasterok, D., Gard, M., & Webb, J. (2018). On the radiogenic heat production of metamorphic,
692 igneous, and sedimentary rocks. *Geoscience Frontiers*, 9(6), 1777–1794.
693 <https://doi.org/10.1016/j.gsf.2017.10.012>
- 694 Hirth, G., & Beeler, N. M. (2015). The role of fluid pressure on frictional behavior at the base of
695 the seismogenic zone. *Geology*, 43(3), 223–226. <https://doi.org/10.1130/G36361.1>
- 696 Hyndman, R. J., & Fan, Y. (1996). Sample Quantiles in Statistical Packages. *American
697 Statistician*, 50(4), 361–365. <https://doi.org/10.1080/00031305.1996.10473566>

- 698 International Seismological Centre (2022). On-line Bulletin. DOI: 10.31905/D808B830
- 699 Jacquey, A. B. & Cacace, M. (2017). GOLEM, a MOOSE-based application v1.0. Zenodo.
700 <http://doi.org/10.5281/zenodo.999401>.
- 701 Kanamori, H. (1977). The energy release in great earthquakes, 82(20), 2981–2987.
- 702 Kellogg, J. N., Camelio, G. B. F., & Mora-Páez, H. (2019). *Cenozoic tectonic evolution of the*
703 *North Andes with constraints from volcanic ages, seismic reflection, and satellite geodesy.*
704 *Andean Tectonics*. Elsevier Inc. <https://doi.org/10.1016/b978-0-12-816009-1.00006-x>
- 705 Kennan, L., & Pindell, J. L. (2009). Dextral shear, terrane accretion and basin formation in the
706 Northern Andes: best explained by interaction with a Pacific-derived Caribbean Plate?
707 *Geological Society, London, Special Publications*, 328(1), 487–531.
708 <https://doi.org/10.1144/SP328.20>
- 709 Kerr, A. C. (2014). Oceanic Plateaus. In *Treatise on Geochemistry: Second Edition* (2nd ed., Vol.
710 4, pp. 631–667). Oxford: Elsevier Ltd. [https://doi.org/10.1016/B978-0-08-095975-7.00320-](https://doi.org/10.1016/B978-0-08-095975-7.00320-X)
711 [X](https://doi.org/10.1016/B978-0-08-095975-7.00320-X)
- 712 Klitzke, P., Luzi-Helbing, M., Schicks, J. M., Cacace, M., Jacquey, A. B., Sippel, J., et al. (2016).
713 Gas hydrate stability zone of the Barents Sea and Kara Sea region. *Energy Procedia*, 97, 302–
714 309. <https://doi.org/10.1016/j.egypro.2016.10.005>
- 715 Laske, G., Masters, G., Ma, Z., & Pasyanos, M. E. (2013). CRUST1.0: An Updated Global Model
716 of Earth's Crust. *Geophys. Res. Abstracts*, 15, Abstract EGU2013--2658. Retrieved from
717 <http://igppweb.ucsd.edu/~gabi/rem.html>
- 718 Li, Y., & Toksoz, N. (1993). Study of the source process of the 1992 Colombia Ms=7.3 earthquake
719 with the empirical Green's function method. *Geophysical Research Letters*, 20(11), 1087–
720 1090.
- 721 Lucazeau, F. (2019). Analysis and mapping of an updated terrestrial heat flow data set.
722 *Geochemistry, Geophysics, Geosystems*, 4001–4024. <https://doi.org/10.1029/2019gc008389>
- 723 Marcaillou, B., Charvis, P., & Collot, J. Y. (2006). Structure of the Malpelo Ridge (Colombia)
724 from seismic and gravity modelling. *Marine Geophysical Research*, 27(4), 289–300.
725 <https://doi.org/10.1007/s11001-006-9009-y>
- 726 Marone, C., & Saffer, D. M. (2015). *The Mechanics of Frictional Healing and Slip Instability*
727 *During the Seismic Cycle. Treatise on Geophysics: Second Edition* (Vol. 4). Elsevier B.V.
728 <https://doi.org/10.1016/B978-0-444-53802-4.00092-0>
- 729 Marone, Chris, & Scholz, C. H. (1988). The depth of seismic faulting and the upper transition from

- 730 stable to unstable slip regimes. *Geophysical Research Letters*, 15(6), 621–624.
731 <https://doi.org/10.1029/GL015i006p00621>
- 732 Martínez, J. M., Parra, E., Paris, G., Forero, C., Bustamante, M., Cardona, O. D. & Jaramillo, J.
733 D. (1994). Los sismos del Atrato Medio 17 y 18 de Octubre de 1992 Noroccidente de
734 Colombia. *Revista Ingeominas*, 4, 35–76.
- 735 McKenzie, D., Jackson, J., & Priestley, K. (2005). Thermal structure of oceanic and continental
736 lithosphere. *Earth and Planetary Science Letters*, 233(3–4), 337–349.
737 <https://doi.org/10.1016/j.epsl.2005.02.005>
- 738 Meeßen, C. (2017). VelocityConversion. GFZ Data Services.
739 <https://doi.org/http://doi.org/10.5880/GFZ.6.1.2017.001>
- 740 Montes, C., Rodriguez-Corcho, A. F., Bayona, G., Hoyos, N., Zapata, S., & Cardona, A. (2019).
741 Continental margin response to multiple arc-continent collisions: The northern Andes-
742 Caribbean margin. *Earth-Science Reviews*, 198(July), 102903.
743 <https://doi.org/10.1016/j.earscirev.2019.102903>
- 744 Mora-Bohórquez, J. A., Oncken, O., Le Breton, E., Mejia-Ibañez, M., Veloza, G., Mora, A., et al.
745 (2020). Formation and Evolution of the Lower Magdalena Valley Basin and San Jacinto Fold
746 Belt of Northwestern Colombia: Insights from Upper Cretaceous to Recent Tectono-
747 Stratigraphy. In J. Gómez & D. Mateus-Zabala (Eds.), *The Geology of Colombia, Volume 3*
748 *Paleogene – Neogene. Servicio Geológico Colombiano, Publicaciones Geológicas*
749 *Especiales*. (Vol. 3, pp. 21–66). <https://doi.org/10.32685/pub.esp.37.2019.02.21>
- 750 Mora, J. A., Oncken, O., Le Breton, E., Ibáñez-Mejia, M., Faccenna, C., Veloza, G., et al. (2017).
751 Linking Late Cretaceous to Eocene tectonostratigraphy of the San Jacinto fold belt of NW
752 Colombia with Caribbean plateau collision and flat subduction. *Tectonics*, 36(11), 2599–
753 2629. <https://doi.org/10.1002/2017TC004612>
- 754 Mosquera-Machado, S., Lalinde-Pulido, C., Salcedo-Hurtado, E., & Michetti, A. M. (2009).
755 Ground effects of the 18 October 1992, Murindo earthquake (NW Colombia), using the
756 Environmental Seismic Intensity Scale (ESI 2007) for the assessment of intensity. *Geological*
757 *Society Special Publication*, 316, 123–144. <https://doi.org/10.1144/SP316.7>
- 758 Muñoz Sabater, J., (2019): ERA5-Land monthly averaged data from 1981 to present. Copernicus
759 Climate Change Service (C3S) Climate Data Store (CDS). (Accessed on 15-09-2019),
760 [10.24381/cds.68d2bb3](https://doi.org/10.24381/cds.68d2bb3)
- 761 Neill, I., Kerr, A. C., Hastie, A. R., Stanek, K.-P., & Millar, I. L. (2011). Origin of the Aves Ridge
762 and Dutch-Venezuelan Antilles: interaction of the Cretaceous “Great Arc” and Caribbean-
763 Colombian Oceanic Plateau? *Journal of the Geological Society*, 168(2), 333–348.
764 <https://doi.org/10.1144/0016-76492010-067>

- 765 Noriega-Londoño, S., Restrepo-Moreno, S. A., Vinasco, C., Bermúdez, M. A., & Min, K. (2020).
 766 Thermochronologic and geomorphometric constraints on the Cenozoic landscape evolution
 767 of the Northern Andes: Northwestern Central Cordillera, Colombia. *Geomorphology*, 351.
 768 <https://doi.org/10.1016/j.geomorph.2019.106890>
- 769 Oleskevich, D., Hyndman, R., & Wang, K. (1999). The updip and downdip limits to great
 770 subduction earthquakes: Thermal and structural models of Cascadia, south Alaska, SW Japan,
 771 and Chile. *Journal of Geophysical Research*, 104(B7), 14965–14991.
- 772 Pagani, M., García-Pelaez, J., Gee, R., Johnson, K., Poogi, R., Styron, G., et al. (2018). Global
 773 Earthquake Model (GEM) Seismic Hazard Map (version 2018.1 - December 2018).
 774 <https://doi.org/10.13117/GEM-GLOBAL-SEISMIC-HAZARD-MAP-2018.1>
- 775 Paris, G., Machette, M. N., Dart, R. L., & Haller, K. M. (2000). *Map and database of Quaternary*
 776 *faults and folds in Colombia and its offshore regions*.
- 777 Pavlis, N. K., Holmes, S. A., Kenyon, S. C., & Factor, J. K. (2012). The development and
 778 evaluation of the Earth Gravitational Model 2008 (EGM2008). *Journal of Geophysical*
 779 *Research: Solid Earth*, 117(4), 1–38. <https://doi.org/10.1029/2011JB008916>
- 780 Pousse-Beltran, L., Vassallo, R., Audemard, F., Jouanne, F., Oropeza, J., Garambois, S., & Aray,
 781 J. (2018). Earthquake geology of the last millennium along the Boconó Fault, Venezuela.
 782 *Tectonophysics*, 747–748(January), 40–53. <https://doi.org/10.1016/j.tecto.2018.09.010>
- 783 Poveda, E., Monsalve, G., & Vargas, C. (2015). Receiver functions and crustal structure of the
 784 northwestern Andean region, Colombia. *Journal of Geophysical Research: Solid Earth*,
 785 (120), 2408–2425. <https://doi.org/10.1002/2014JB011304>.
- 786 Poveda, E., Julià, J., Schimmel, M., & Perez-Garcia, N. (2018). Upper and Middle Crustal Velocity
 787 Structure of the Colombian Andes From Ambient Noise Tomography: Investigating
 788 Subduction-Related Magmatism in the Overriding Plate. *Journal of Geophysical Research:*
 789 *Solid Earth*, 123(2), 1459–1485. <https://doi.org/10.1002/2017JB014688>
- 790 Reguzzoni, M., & Sampietro, D. (2015). GEMMA: An Earth crustal model based on GOCE
 791 satellite data. *International Journal of Applied Earth Observation and Geoinformation*,
 792 35(PA), 31–43. <https://doi.org/10.1016/j.jag.2014.04.002>
- 793 Restrepo, J. J., & Toussaint, J. F. (1988). Terranes and continental accretion in the Colombian
 794 Andes. *Episodes*, 11(3), 189–193. <https://doi.org/10.18814/epiiugs/1988/v11i3/006>
- 795 Rodriguez Picada, C., Scheck-Wenderoth, M., Cacace, M., Bott, J., & Strecker, M. R. (2022).
 796 Long-Term Lithospheric Strength and Upper-Plate Seismicity in the Southern Central Andes,
 797 29°–39°S. *Geochemistry Geophysics Geosystems*, 23(e2021GC010171).
 798 <https://doi.org/10.1029/2021GC010171>

- 799 Salazar, W., Brown, L., Hernández, W., & Guerra, J. (2013). An Earthquake Catalogue for El
800 Salvador and Neighboring Central American Countries (1528-2009) and Its Implication in
801 the Seismic Hazard Assessment. *Journal of Civil Engineering and Architecture*, 7(8), 1018–
802 1045. <https://doi.org/10.17265/1934-7359/2013.08.011>
- 803 Schaeffer, A. J., & Lebedev, S. (2013). Global shear speed structure of the upper mantle and
804 transition zone. *Geophysical Journal International*, 194(1), 417–449.
805 <https://doi.org/10.1093/gji/ggt095>
- 806 Scheck-Wenderoth, M., & Maystrenko, Y. P. (2013). Deep control on shallow heat in sedimentary
807 basins. *Energy Procedia*, 40, 266–275. <https://doi.org/10.1016/j.egypro.2013.08.031>
- 808 Scholz, C. H. (2019). *The Mechanics of Earthquakes and Faulting*. Cambridge University Press
809 (3rd Edition). Cambridge University Press.
- 810 Sibson, R. (1982). Fault zone models, heat flow, and the depth distribution of earthquakes in the
811 continental crust of the United States. *Bull. Seismol. Soc. Am.*, 72(1), 151–163.
- 812 Silva, V., Amo-Oduro, D., Calderon, A., Dabbeek, J., Despotaki, V., Martins, L., et al. (2018).
813 Global Earthquake Model (GEM) Seismic Risk Map (version 2018.1).
814 <https://doi.org/10.13117/GEM-GLOBAL-SEISMIC-RISK-MAP-2018>
- 815 Storchak, D. A., Harris, J., Brown, L., Lieser, K., Shumba, B., & Di Giacomo, D. (2020). Rebuild
816 of the Bulletin of the International Seismological Centre (ISC)—part 2: 1980–2010.
817 *Geoscience Letters*, 7(1). <https://doi.org/10.1186/s40562-020-00164-6>
- 818 Styron, R., García-Pelaez, J., & Pagani, M. (2020). CCAF-DB: The Caribbean and Central
819 American active fault database. *Natural Hazards and Earth System Sciences*, 20(3), 831–857.
820 <https://doi.org/10.5194/nhess-20-831-2020>
- 821 Sun, M., Bezada, M. J., Cornthwaite, J., Prieto, G. A., Niu, F., & Levander, A. (2022). Overlapping
822 slabs: Untangling subduction in NW South America through finite-frequency teleseismic
823 tomography. *Earth and Planetary Science Letters*, 577, 117253.
824 <https://doi.org/10.1016/j.epsl.2021.117253>
- 825 Tse, S. T., & Rice, J. R. (1986). Crustal earthquake instability in relation to the depth variation of
826 frictional slip properties. *Journal of Geophysical Research*, 91(B9), 9452.
827 <https://doi.org/10.1029/jb091ib09p09452>
- 828 Turcotte, D., & Schubert, G. (2002). *Geodynamics*. Cambridge.
829 <https://doi.org/10.1017/CBO9781107415324.004>
- 830 Veloza, G., Styron, R., & Taylor, M. (2012). Open-source archive of active faults for northwest
831 South America. *GSA Today*, 22(10), 4–10. <https://doi.org/10.1130/GSAT-G156A.1>

- 832 Vilà, M., Fernández, M., & Jiménez-Munt, I. (2010). Radiogenic heat production variability of
833 some common lithological groups and its significance to lithospheric thermal modeling.
834 *Tectonophysics*, 490(3–4), 152–164. <https://doi.org/10.1016/j.tecto.2010.05.003>
- 835 Weatherall, P., Marks, K. M., Jakobsson, M., Schmitt, T., Tani, S., Arndt, J. E., et al. (2015). A
836 new digital bathymetric model of the world's oceans. *Earth and Space Science*, 2, 331–345.
837 <https://doi.org/10.1002/2015EA000107>
- 838 Wessel, P. & Smith, W. H. F. (1991). Free software helps map and display data, EOS Trans. AGU,
839 72, 441.
- 840 Wiemer, S., & Wyss, M. (2000). Minimum magnitude of completeness in earthquake catalogs:
841 Examples from Alaska, the Western United States, and Japan. *Bulletin of the Seismological*
842 *Society of America*, 90(4), 859–869. <https://doi.org/10.1785/0119990114>
- 843 Wiemer, Stefan, & Wyss, M. (1997). Mapping the frequency-magnitude distribution in asperities:
844 An improved technique to calculate recurrence times? *Journal of Geophysical Research:*
845 *Solid Earth*, 102(B7), 15115–15128. <https://doi.org/10.1029/97jb00726>
- 846 Woessner, J., & Wiemer, S. (2005). Assessing the quality of earthquake catalogues: Estimating
847 the magnitude of completeness and its uncertainty. *Bulletin of the Seismological Society of*
848 *America*, 95(2), 684–698. <https://doi.org/10.1785/0120040007>
- 849 Wu, W. N., Yen, Y. T., Hsu, Y. J., Wu, Y. M., Lin, J. Y., & Hsu, S. K. (2017). Spatial variation
850 of seismogenic depths of crustal earthquakes in the Taiwan region: Implications for seismic
851 hazard assessment. *Tectonophysics*, 708, 81–95. <https://doi.org/10.1016/j.tecto.2017.04.028>
- 852 Zielke, O., Schorlemmer, D., Jónsson, S., & Mai, P. M. (2020). Magnitude-dependent transient
853 increase of seismogenic depth. *Seismological Research Letters*, 91(4), 2182–2191.
854 <https://doi.org/10.1785/0220190392>
- 855 Zuza, A. V., & Cao, W. (2020). Seismogenic thickness of California: Implications for thermal
856 structure and seismic hazard. *Tectonophysics*, 782–783(April), 228426.
857 <https://doi.org/10.1016/j.tecto.2020.228426>